1   **Structural basis for acyl chain control over glycosphingolipid sorting and vesicular trafficking**

2

3   Stefanie S. Schmieder[1], Raju Tatituri[2,3], Michael Anderson[1,4], Kate Kelly[1], and Wayne I.

4   Lencer[1,3,4*]

5   1 Division of Gastroenterology, Boston Children's Hospital, Boston MA 02115

6   2 Division of Rheumatology, Brigham and Women's Hospital, Boston MA 02115

7   3 Harvard Medical School, Boston MA 02115

8   4 Harvard Digestive Diseases Center, Boston, MA 02115

9   *Corresponding author

10

11   **Abstract**

12   The complex sphingolipids exhibit a diversity of ceramide acyl chain structures that influence their

13   trafficking and intracellular distributions, but how the cell discerns among the different ceramides to

14   affect such sorting remains unknown. To address mechanism, we synthesized a library of GM1

15   glycosphingolipids with naturally varied acyl chains and quantitatively assessed their sorting among

16   different endocytic pathways. We found that a stretch of at least 14 saturated carbons extending from

17   C1 at the water-bilayer interface dictated lysosomal sorting by exclusion from endosome sorting

18   tubules. Sorting to the lysosome by the C14*-motif was cholesterol dependent. Perturbations of the

19   C14*-motif by unsaturation enabled GM1 entry into endosomal sorting tubules of the recycling and

20   retrograde pathways independently of cholesterol. Unsaturation occurring beyond the C14*-motif in

21   very long acyl chains rescued lysosomal sorting. These results define a structural motif underlying

22   membrane organization of sphingolipids and implicate cholesterol-sphingolipid nanodomain formation

23   in sorting mechanisms.

24

Introduction

Membrane function depends on the structural variations and dynamic physical properties of the acyl chains that form each class of its lipid components. But how the acyl chains operate to differentially affect the membrane biology of a lipid, and why so many different acyl chain structures are conserved within each lipid species remain in large part unexplained.

The complex sphingolipids, comprised of the glycosphingolipids (GSLs) and sphingomyelin, constitute 10-20 mole % of plasma membrane lipids (*1, 2*), and they provide a tractable experimental system to examine how acyl chain structure affects lipid function. In many cases, the activities of complex glycosphingolipids appear to depend upon locally segregating into liquid-liquid phase-separated nanodomains that form upon close interactions with cholesterol (*3-6*), the cortical cytoskeleton (*7-11*), and other scaffolding proteins (*12-14*). This is the lipid-raft or lipid nanodomain hypothesis (*15-20*). Considerable evidence shows that nanodomains are critical for key cellular processes including membrane protein trafficking, signal transduction, and receptor cell surface distributions (*16, 21-27*). Because of their functions in vesicular trafficking, some GSLs forming membrane nanodomains are co-opted by viruses and toxins, and by endogenous lectins, as platforms for entry into the cell and causation of disease (*28-34*).

Here, we studied ganglioside GM1, the glycosphingolipid receptor that mediates cholera toxin (CTx) entry into host cells. GM1 typifies the complex sphingolipids in basic structure and function. The different GM1 species, like all other complex sphingolipids, are comprised of a hydrophilic extracellular moiety (a specific pentasaccharide for GM1, one or more sugars for the other GSLs, and phosphocholine for sphingomyelin) coupled to a ceramide that anchors the molecule in the membrane. The ceramide moieties consist of a sphingosine base (predominantly 18 hydrocarbons long, C18:1$^{\Delta 4}$, *trans*) linked to a fatty acid by an amide bond to the C1 carbon positioned at the lipid bilayer-water interface. The sphingosine base varies in structure only to a small degree, but the acyl chain can display considerable heterogeneity in both length (C14 to C26) and saturation (single *cis* or no double bond) (*35, 36*). Because these lipids contain large hydrophilic extracellular head groups, they are trapped in the outer leaflet

53   of the membrane bilayer and their distribution throughout the cell occurs only by vesicular

54   traffic (*37, 38*). This can be quantitatively measured and compared for GM1 species with

55   identical head groups but with varied acyl chains in their ceramide moieties.

56   We previously found the different acyl chains in the ceramide moiety of GM1 act decisively in

57   trafficking the toxin into the different endocytic and sub-cellular compartments required for the

58   induction of toxicity (*39, 40*). GM1 species containing ceramides with "kinked" shapes caused

59   by a *cis*-double bond in the acyl chains (C16:1$^{\Delta 9}$ or C18:1$^{\Delta 9}$) sorted into the recycling and

60   retrograde endosome pathways, and GM1 species containing ceramides with saturated acyl

61   chains of the same length, C16:0 and C18:0, but with "straight conical" shapes, sorted to the

62   lysosome instead (*40*). Additional evidence that acyl chain structure of the complex

63   sphingolipids may affect trafficking was recently shown for ceramide-anchored proteins in the

64   biosynthetic pathway of yeast (*41*). But how the cell discerns among the different ceramide

65   moieties to affect this acyl chain-based sorting has not been explained.

66   To address these problems, we synthesized a library of eleven GM1 species with ceramides

67   reflecting the naturally occurring variations of fatty acyl chain length and saturation. This

68   provided a direct test of GSL structural biology in ways not previously possible.

69   In mammals, the single *cis*-double bond in the acyl chain of the unsaturated ceramide is created

70   by palmityl/stearoyl-CoA desaturase (SCD). The enzyme installs a *cis*-double bond invariably at

71   the Δ^9-position of C16:0 or C18:0 fatty acids, creating a 'kinked' shaped lipid (*42*). When

72   coupled to sphingosine by the ceramide synthases, and then incorporated into the complex

73   sphingolipids, the kink in the acyl chain of these ceramide species is positioned where it should

74   impair close packing against the rigid planar surface of cholesterol (*43*). On the other hand, GSL

75   species containing ceramides with longer unsaturated acyl chains will have the *cis*-double

76   bonds placed deeper within the membrane bilayer. They are built upon the same C18:1 acyl

77   chains generated by the Δ9-desaturase, but lengthened at the carboxy-terminus by the ELOVL

78   elongases (*44*). Consequently these unsaturated very long acyl chains contain longer stretches

79   of saturated hydrocarbons extending from the water-bilayer interface into the membrane

80   bilayer. In some cases, the *cis*-double bond will be positioned beyond the planar surface of

81   cholesterol. We reasoned that these unsaturated, and "kinked", very long acyl chain GSLs might

82   still assemble closely with cholesterol to form nanodomains and function accordingly - thus

83   providing a structural test of sphingolipid behavior in live cells.

84   Our results define a structural motif in the ceramide acyl chain of the GSLs that dictates

85   endosomal sorting and with broad implications for current models of membrane structure and

86   function.

87

88 **Results**

89 The eleven GM1 molecules synthesized for testing contained saturated and mono-unsaturated

90 acyl chains (Fig. 1B) produced naturally in mammalian cells (*45, 46*). Three additional molecules,

91 the GM1 C12:1$^{\Delta 6}$, C12:0, and C16:1$^{\Delta 9}$ species, were prepared to contain non-native ceramide

92 acyl chains that broadened the testing of the hypothesis (Fig. 1B, Suppl. Fig. 1A). The cellular

93 and membrane behaviors of each GM1 species were studied by coupling the extracellular

94 oligosaccharide to a 'reporter'-peptide containing biotin and fluorophore (Suppl. Fig. 1A), or

95 directly to a fluorophore (*40, 47, 48*).

96 As a first test of membrane behavior, the liquid ordered (L_o) and liquid disordered (L_d) phase

97 preferences for each of the GM1 species were defined *in vitro* using giant plasma membrane

98 vesicles (GPMVs) prepared from different cell lines as indicated (Suppl. Figs. 1B – D). Certain

99 saturated lipids and sterols can condense into higher ordered assemblies within membranes,

100 termed the L_o phase. This separates them from the other lipids present in the same membrane

101 termed the L_d phase. Phase partitioning into the L_o phase can be considered a feature of

102 nanodomains in live cells (*49, 50*). We found the major determinant for the phase behaviors of

103 the different GM1 species in GMPVs to be the presence or absence of a *cis*-double bond in the

104 ceramide acyl chain. The unsaturated GM1 species segregated into the L_d phase irrespective of

105 the cell type-specific GMPV tested. GM1 with fully saturated ceramide acyl chains associated

106 exclusively with the L_o phase. Thus, partitioning into the L_o phase in GPMVs depended on full

107 saturation of the fatty acyl chain.

108 **A saturated acyl chain length of at least 14 carbon atoms in the GM1 ceramide directs sorting**

109 **to the lysosome**

110 We next used lattice light-sheet and airyscan microscopy to image the different fluorescently-

111 labeled GM1 species in the sorting endosome and their ability to enter endosomal sorting

112 tubules. Endosomal sorting tubules affect the trafficking of membrane and cargo away from the

113 lysosome and into the recycling pathway for return back to the plasma membrane (PM), or into

114 the retrograde pathway for transport to Golgi and endoplasmic reticulum (ER) (schematic, Fig.

115   1A). For these studies, human A431 epithelial cells were co-incubated with nM concentrations

116   of the different GM1 species together with transferrin (Tfn) and dextran. Tfn and dextran were

117   used to mark the endosome recycling and the lysosome pathways respectively (*51, 52*). Sorting

118   endosomes, which serve all pathways, were operationally defined as Tfn and dextran double

119   positive vesicles, and sorting tubules emerging from these structures were identified by their

120   Tfn-only content. We tested several cell lines for this assay. The A431 cell line selected for these

121   studies exhibited highly elongated and easily visualized tubules emerging from the sorting

122   endosome. The same basic phenotypes, however, were observed in other A431 clones, and

123   HeLa (Suppl. Fig 1D and E), MDCK II, Caco2, and HT29 cell lines which all lacked the unusually

124   elongated tubules (data not shown).

125   We found that the GM1 species with ceramides containing short saturated acyl chains ($\leq$ C14:0)

126   or unsaturated acyl chains C12:1$^{\Delta6}$ through C22:1$^{\Delta13}$ efficiently co-localized with Tfn in

127   endosome sorting tubules (Fig. 1C, left panels and quantified in Fig. 1E and Suppl. Video 1). The

128   GM1 species with ceramides containing long saturated acyl chains $\geq$ C16:0, however, did not

129   (Fig. 1C, right panels, Fig. 1E and Suppl. Video 2). They were localized only to the body of the

130   sorting endosome. We tested this observation again using the C18:0 and C18:1 ceramide pair

131   loaded together into the same cells and obtained the same results (Fig. 1D and 1F and Suppl.

132   Video 2).

133   Notably, we also found that the GM1 species containing ceramides with unsaturated but very

134   long acyl chains ($\geq$ C24:1$^{\Delta15}$ in length) were localized only in the body of the sorting endosome,

135   behaving like the GM1 species with fully saturated acyl chains. These GSLs did not enter the

136   narrow highly-curved sorting tubules despite the presence of a *cis*-double bond in their

137   ceramide acyl chain (Fig. 1B, 1C lower right panels, and Fig. 1E). Additionally, the GM1 species

138   with C14:0 or C22:1$^{\Delta13}$ fatty acids displayed intermediate and closely similar phenotypes. They

139   still entered endosome sorting tubules but less efficiently (measured as lower fluorescence

140   intensity in recycling endosomal tubules) (Fig. 1G and H left panel). This observation was not

141   explained by reduced endocytic uptake of the lipids (Fig. 1H right panel). Closely similar

142   phenotypes for all the GM1 species tested were found in Hela cells (Suppl. Fig. 1E and F), and

6

143 for the other epithelial cell lines noted above (data not shown). Thus, while the presence or

144 absence of a *cis*-double bond in the ceramide acyl chain dictated L_o and L_d phase partitioning in

145 GMPVs, the position of the double bond within the acyl chain acted as the decisive factor for

146 endosomal sorting in live cells. Lipid shape, on its own, was not sufficient to explain the

147 differential sorting observed. These results, especially considering the intermediate behaviors

148 of the C14:0 and C22:1$^{\Delta 13}$ ceramide species, showed that a saturated acyl chain length of at

149 least 14 carbon atoms plus one, extending from the C1 amide bond at the water-bilayer

150 interface, was necessary for retention of GM1 in the body of the endosome. We henceforth

151 name this structure the C14*-motif (Fig. 1G).

Independence from Lectin binding

153 The C14*-motif may be necessary but not sufficient to explain the differential endosomal

154 sorting of GM1 as endogenous lectins capable of scaffolding the lipid may be involved (*34*).

155 Such an effect on GM1 trafficking is perhaps best typified by multi-valent binding to CTxB (*33,*

156 *40, 53-55*). As such, we first tested if binding CTxB might act on the different GM1 species to

157 affect changes in their L_d and L_o phase behaviors as assessed in GMPVs. The addition of CTxB

158 caused a switch from L_d to L_o phase preference, but only for the GM1 species with very long

159 unsaturated acyl chains ≥ 22:1$^{\Delta 13}$ (Suppl. Fig.1G). The phase preferences for the other GM1

160 species were not affected.

161 To test if in live cells cross-linking GM1 by endogenous lectins may be required for its

162 endosomal sorting, we studied the GM1 C16:0 and C16:1$^{\Delta 9}$ pair, and GM1 C24:1$^{\Delta 15}$. Here,

163 intracellular trafficking of the different GM1 species was studied in A431 cells continuously

164 exposed to 100 mM lactose or sucrose to compete against binding the GM1 oligosaccharide

165 moiety by endogenous lectins (*56*). We found no effect of the disaccharide treatments (Suppl.

166 Fig. 1H). Control studies showed that 100 mM lactose was sufficient to block the high affinity

167 binding of CTxB to GM1 on the A431 cell surface (Suppl. Fig.1I). Thus, binding by endogenous

168 galactose- or glucose-binding lectins does not appear to be required for the observed GM1

169 endosomal sorting (Fig. 1B) - in these cases, the C14*-motif is both necessary and sufficient.

7

Differential sorting between the lysosomal and recycling pathways

To quantitatively test if endosomal GM1 sorting is based on the C14* motif, we developed a FACS based assay to measure GM1 sorting between recycling endosomes and lysosomes (Fig. 1A, Pathways A vs C). For these studies, we synthesized the GM1 library coupled to the all-D amino acid 'reporter'-peptide containing only a biotin functional group (Suppl. Fig. 1A). Conditions for incorporating the different GM1 species into the PM at similar amounts were determined experimentally (Fig. 2A, left panel). After a 3h 'chase', the amount of the biotin-labeled-GM1 located at the cell surface was determined by FACS measured by binding of fluorescently-labeled streptavidin (Fig. 2A and 2B). We found that the GM1 species which entered endosome sorting tubules and lacked the C14* motif (GM1 C12:0, C14:0, C16:1$^{\Delta 9}$, C18:1$^{\Delta 9}$ and C22:1$^{\Delta 13}$, Figs. 1E and 2A and B magenta points) were recycled after endocytosis. They were detected on the PM at significantly higher levels compared to the GM1 species containing the C14*-motif (GM1 C16:0, C18:0, C24:1$^{\Delta 15}$, C24:0 and C26:1$^{\Delta 17}$, Fig. 2A and 2B turquoise points). Even after longer chase times (> 6 h), the GM1 C16:1$^{\Delta 9}$ species still localized to the PM and within endosomal recycling tubules containing Tfn; while the GM1 C16:0 species localized strictly to intracellular vesicles stained by lysotracker™ (marking late endosomes and lysosomes, Suppl. Fig. 2A). We observed no confounding effects of GM1 treatment on endocytosis per se - as measured by dextran (fluid-phase) or Tfn (receptor-mediated) uptake (Suppl. Fig. 2B). In addition, the results could not be simply explained by differential endocytic uptake mechanisms into caveolae - as neither the C18:1$^{\Delta 9}$ nor C18:0 species were sensitive to CRISPR-Cas9 deletion of cavin1 (Suppl. 2C). Thus, a saturated acyl chain length of at least 14 saturated carbon atoms plus one (the C14*-motif) drives endosomal sorting of GM1 to the lysosome, with GM1 C14:0 and C22:1$^{\Delta 13}$ displaying intermediate phenotypes (Fig. 1A pathway C, and Fig. 2C). We note again that lysosomal sorting was rescued for the unsaturated GM1 species containing very long unsaturated acyl chains (i.e. unsaturated "kinked shaped" fatty acids containing the C14*-motif").

Cholesterol Dependence for Sorting to the Lysosome

197 The nanodomain (lipid raft) hypothesis posits strong dependence on close assembly between
198 GSLs and membrane cholesterol. We reasoned, however, that such cholesterol dependence
199 should be evident for endosomal sorting of only the GM1 species with ceramide structures
200 containing the C14*-motif - if the motif acts as we hypothesize by allowing close alignment
201 against the rigid and flat surface of cholesterol (*3, 6, 43*). Likewise, endosomal sorting of the
202 GM1 species with *cis*-double bonds at positions disrupting the C14*-motif should behave
203 independently of membrane cholesterol. But the GM1 species with a *cis*-double bond located
204 beyond the C14*-motif, as seen in the naturally occurring very long acyl chains (> C22:1$^{\Delta13}$ acyl
205 chains), should again show cholesterol-dependence.

206 To test this idea, we studied the endosome recycling of the different GM1 species in A431 cells
207 mildly reduced of membrane cholesterol: either by treatment with low doses of the small
208 molecule inhibitors of cholesterol metabolism simvastatin, T0901317, or U18666A; or as we
209 found experimentally by CRISPR-Cas9 knock out of serine-palmityltransferase-2 (SPTLC-2),
210 ceramide synthase 5 (CerS5), or ceramide synthase 2 (CerS2), or by simply growing the cells in
211 over-confluent conditions. In all cases, the experimental conditions were found to lower plasma
212 membrane cholesterol content as measured by loss of filipin staining (Suppl. Fig. 2D, left panel),
213 and further evidenced by increase in the general polarization (GP) of laurdan as assessed in
214 GPMVs (implicating increased membrane fluidity typifying cholesterol depleted membranes,
215 Suppl. Fig. 2D, right panel). We also conducted lipidomic profiling by mass spectrometry, which
216 showed in all cases that cells depleted of cholesterol had only minor changes in the different
217 species of the major membrane lipid classes: phosphatidylethanolamine (PE),
218 phosphatidylglycerol (PG), and phosphatidylcholine (PC) (Suppl. Fig. 3D). Additionally, and in all
219 cases, cells depleted in cholesterol by our methods retained their normal endosomal and
220 overall morphologies and endocytic uptake rates with only minor variations (Fig. 2E left panel
221 and Suppl. Fig. 2E). We also note that cholesterol depletion induced by over-confluent cell
222 culture, the least invasive perturbation, had only minimal effects on the overall lipidome and no
223 detectable changes on phase preferences for any of the different GM1 species in GPMVs
224 (Suppl. Fig. 2H).

225   Consistently, for all methods, we found no effect of cholesterol depletion on the recycling of

226   GM1 species lacking the C14*-motif (Fig. 2D magenta points, and Suppl. Fig. 2F, left table). In

227   contrast, cholesterol depletion uniformly affected the late endosome/lysosome sorting of GM1

228   species with ceramide moieties containing the C14*-motif. This included the saturated acyl

229   chains ≥ C16:0 and notably the unsaturated ceramides with very long unsaturated acyl chains ≥

230   C24:1$^{\Delta 15}$. In cholesterol depleted cells, these GM1 species were no longer strictly sorted into

231   the late endosome/lysosome - instead, large fractions of these lipids were recycled back to the

232   PM (Fig. 2D turquoise points and Suppl. Fig. 2F, right table) and co-localized within Tfn-

233   containing endosome recycling tubules (where none was found before) (Fig. 2F and G). The

234   effect of cholesterol depletion on lysosomal sorting was specific for GM1, as lysosomal sorting

235   for the epidermal growth factor (EGF) receptor or the low density lipoprotein receptor LDL-R

236   were not affected (Fig. 2E right panel and Suppl. Fig. 2G). Thus, the sorting step for trafficking

237   GM1 into the lysosome appears to be dependent on membrane cholesterol, but only for the

238   GM1 species with ceramide structures containing the C14*-motif and predicted to interface

239   tightly alongside the sterol - consistent with the nanodomain hypothesis.

240   **Sorting into retrograde and recycling pathways by bulk membrane flow**

241   We next considered the possibility that the GM1 species lacking the C14*-motif may enter

242   endosome sorting tubules by default, following bulk membrane flow (*57*). If this were the case,

243   we reasoned these GM1 species should enter all pathways emerging from the sorting

244   endosome, including the retrograde pathway to the trans Golgi and ER. For these studies, we

245   used the B-subunit of cholera toxin (CTxB). Though CTxB scaffolds GM1 into a multimeric

246   complex affecting its membrane behavior (*54, 58, 59*), ceramide structure still plays a decisive

247   role in endosomal sorting into the ER (*40*) and in liquid phase partitioning in GMPVs (Suppl. Fig.

248   1G). For these studies, the different GM1 species were applied to a HeLa cell line that

249   endogenously lacks GM1. CTxB trafficking into the ER was quantitatively measured using a

250   FACS-based split-GFP assay recently developed by our group (*60*). We found that only the short

251   chain (≤ C14:0) or unsaturated GM1 species (≤ C22:1$^{\Delta 13}$), both lacking the C14*-motif, efficiently

252   trafficked CTxB into the ER (Fig. 3A and 3B). The GM1 species containing the C14*-motif did

253   not. This includes the GM1 species with ceramide structures containing long saturated acyl

254   chains ($\geq$ C16:0), and those containing unsaturated but very long acyl chains ($\geq$ C24:1$^{\Delta15}$), which

255   rescues the C14*-motif and its function. Thus, the requirement for acyl chain structure directing

256   the different GM1 species into the retrograde endosomal pathway phenocopied exactly the

257   structures required for sorting into the recycling pathway.

258   To confirm these results, we took an orthogonal approach and generated A431 cells containing

259   CRISPR-Cas9 deletion of CerS2, the ceramide synthase producing very long acyl chain ceramides

260   (> C20), or deletion of CerS5, the synthase producing ceramides containing short acyl chain

261   ceramides ($\leq$ C16) (*61*). These deletions genetically bias the structures of the endogenous GM1

262   ceramide moieties in CerS2 and CerS5 KO cells as just described. The approach was validated by

263   lipidomic profiling of sphingomyelin (SM). SM and GSLs share the same ceramide biosynthetic

264   pathway and the abundance of SM in cell membranes allowed for the most conclusive analysis

265   of endogenous ceramide structures. In wild type A431 cells, the major SM species contained

266   C18:0 (45%), followed by C24:1 (15-18%), and C18:1 (10%) acyl chains (Suppl. Fig. 3C).

267   Sphingomyelin containing ceramides with short acyl chains $\leq$ C16 (6-8%) were also reproducibly

268   detected (n = 8 replicates). As expected in cells lacking CerS2, the SM species most strongly

269   depleted were ceramides containing the very long acyl chains, but with concomitant increase in

270   C18:0 and C18:1; while in cells lacking CerS5, the SM species most strongly depleted were the

271   short acyl chains $\leq$ C16, and unexpectedly the C18 acyl chain species, with increases in C22:0

272   and C24:1.

273   When tested for GM1-dependent trafficking of CTxB, we found that the retrograde pathway

274   was significantly reduced in those cells lacking CerS5 (Fig. 3C), consistent with 1) the loss of the

275   short and C18:1 acyl chain ceramides that lack the C14*-motif; and 2) the increased expression

276   of the very long chain saturated ceramide species C22:0 - including notably again those with an

277   unsaturated bond positioned more deeply in the membrane (GM1 C24:1$^{\Delta15}$) - which contain the

278   C14*-motif. We found a slight increase in retrograde trafficking for cells depleted in Cer2,

279   consistent with depletion of only the very long chain ceramides and the modest increase in

280   ceramides with C18:1$^{\Delta9}$ (Fig. 3C and Suppl. Fig. 3C). Again, control studies showed that

281 endocytosis and EGF/LDL-R trafficking to the lysosome in CerS5 and CerS2 KO cells were not

282 altered, or slightly enhanced (Fig. 2E, Suppl. Fig. 2G).

283 Opposite results were found for sorting CTxB to the acidic lysosome as predicted. This was

284 measured by FACS using CTxB coupled to the pH-sensitive fluorophore pHrodo™. We found

285 that CTxB-pHrodo™ fluorescence was reduced in the A431 cells deleted in CerS2, consistent

286 with loss of very long acyl chain ceramides containing the C14*-motif and increase in the

287 unsaturated C18:1$^{\Delta9}$ ceramide lacking the motif (Fig. 3D). For cells deleted in CerS5, which

288 expressed higher levels of very long acyl chain ceramides (C20:0, C22:0, and C24:1$^{\Delta15}$), we found

289 a slight increase in lysosomal transport - consistent with the enhanced expression of GM1 lipids

290 containing the C14*-motif. Thus, the genetically modified cell lines phenocopied the trafficking

291 of GM1 observed using exogenously applied and structurally defined GM1 species.

292 Cholesterol depletion had the same effect (Fig. 3E) – here we also observed an increase in

293 retrograde trafficking to the ER (Fig. 3F). These results implicate a selective and cholesterol

294 dependent process for retention within the body of the endosome followed by maturation to

295 lysosomes for the GM1 ceramides that contain the C14*-motif (Fig. 3E and 3F). GM1 species

296 lacking the C14*-motif escape this lysosomal sorting step and sort, perhaps passively by

297 following bulk membrane flow, into endosome tubules serving the recycling and retrograde

298 endocytic pathways.

299 **The C14* motif drives nanodomain assembly and segregation at the plasma membrane**

300 The cholesterol dependency observed for C14*-motif based GM1 sorting to the lysosome is

301 consistent with the idea that the mechanism of such sorting may involve assembly into

302 membrane nanodomains. To test this, we imaged the GM1 C18:0 and C18:1$^{\Delta9}$ species in sorting

303 endosomes artificially enlarged to enable visualization by over expression of dominant active

304 Rab5Q79L (tagged with EGFP). We found clear separation of the two GM1 species in the plane

305 of the endosomal membrane (Fig. 4A and B), and clear segregation between GM1 C18:0 (but

306 not GM1 C18:1$^{\Delta9}$) and the Tfn-Tfn-R complex. Again, the unsaturated very long acyl chain GM1

307 C24:1$^{\Delta15}$, which also contains the C14*-motif, was found to behave like GM1 C18:0. These

308   results imply nanodomain formation within the sorting endosome. Notably, the clear

309   segregation of the two unsaturated GM1 species C24:1$^{\Delta15}$ and C18:1$^{\Delta9}$ into distinct endosomal

310   nanodomains in live cells was not predicted by their phase behaviors in GMPVs (Suppl. Fig. 1B -

311   D). In those studies, phase separation was dictated by the presence or absence of *cis*-double

312   bond (kinked or straight shapes). In live cells, as evidenced here, we find the C14*-motif to be

313   the decisive factor - not lipid shape.

314   We were then curious to know if such segregation by nanodomain formation may also occur in

315   the plasma membrane, before the lipids were internalized by endocytosis. To test this, we

316   measured the diffusion rate of GM1 C18:0, C18:1$^{\Delta9}$, and C24:1$^{\Delta15}$ in plasma membranes of A431

317   cells using FRAP. We found slower rates of fluorescence recovery (FRAP) for the GM1 C18:0 and

318   C24:1$^{\Delta15}$ species (which contain the C14*-motif) compared to GM1 C18:1$^{\Delta9}$ species (which lacks

319   the C14*-motif) (Fig. 4C). Thus, even in the plasma membrane, the distinct behaviors among

320   the different GM1 species appears to be dictated by the C14*-motif. The slower diffusion of the

321   GM1 C18:0 and C24:1$^{\Delta15}$ species is consistent with their assembly in membrane nanodomains

322   linked to the subcortical cytoskeleton (*62*).

323   To test if these differences in plasma membrane mobility correlated with differences in uptake,

324   we measured the apparent rate of endocytosis. Here, we used SVGA cells endogenously

325   expressing Rab5-GFP to measure the co-localization between the different GM1 species and

326   Rab5 early endosomes. Uniformly, after short 5 to 10 min incubations, little co-localization with

327   Rab5-endosomes was observed for GM1 ceramides containing fully saturated C16:0, C18:0, and

328   C24:0 acyl chains and for the very long unsaturated acyl chain GM1 C24:1$^{\Delta15}$ (Fig. 4D) These

329   ceramides all contain the C14*-motif. The result implicates slow rates of endocytosis, or very

330   fast transition to Rab 7 late endosomes (or both) for these GM1 species. In contrast, we found a

331   much higher degree of co-localization between the Rab5-endosome and GM1 ceramides

332   containing the C16:1$^{\Delta9}$ and C18:1$^{\Delta9}$ acyl chains, which lack the C14*-motif - consistent with

333   rapid rates of endocytosis, or efficient recycling (or both). The same results were obtained using

334   Tfn, which we used as a control, phenocopying the C16:1$^{\Delta9}$ and C18:1$^{\Delta9}$ GM1 species (Fig. 4D).

335   When the SVGA cells were depleted of cholesterol, however, co-localizations of the GM1 C16:0

336   and very long C24:1$^{\Delta 15}$ acyl chain species with Rab5 endosomes were increased (Fig. 4E). These

337   lipids also displayed an increase in their PM mobility after cholesterol depletion as assessed by

338   FRAP (Fig 4F, compare black with magenta lines and Suppl. Fig. 4A for quantification). When the

339   SVGA cells were supplemented with additional exogenous cholesterol, however, the degree of

340   colocalization with Rab5 endosomes was diminished for the same GM1 C16:0 and C18:0

341   species, and for the very long unsaturated acyl chain C24:1$^{\Delta 15}$ species - compared to control

342   untreated cells (Fig. 4G and Suppl. Fig. 4B). This phenotype induced by cholesterol addition was

343   more readily apparent in HT29 cells, where PM localization was prominently marked at cell-cell

344   contact sites. Here, these lipids appeared to be visibly "trapped" on the PM after cholesterol

345   addition (Fig. 4G and H, and Suppl. Fig. 4D). Notably, the addition of cholesterol to SVGA cells

346   had no detectable effect on the apparent efficiency of co-localization with Rab5-endosomes for

347   the unsaturated GM1 species C16:1$^{\Delta 9}$ and C18:1$^{\Delta 9}$ (all lacking the C14*-motif) or for Tfn used as

348   control. And we found no confounding effect of cholesterol treatment on fluid-phase dextran

349   endocytic uptake or EGF-R/LDL-R sorting to the lysosome (Suppl. Fig. 4F).

350   Further evidence that excess membrane cholesterol caused retention of GM1 species

351   containing the C14*-motif on the PM was obtained in A431 cells as assessed by FACS (Suppl.

352   Fig. 4E) and by confocal microscopy (Fig. 4H). - and with no evidence for co-localization within

353   Tfn-positive endosome recycling tubules (Suppl. Fig. 4D). We also found a striking reduction in

354   PM diffusion rates for the C18:0 and C24:1$^{\Delta 15}$ species in A431 cells treated with exogenous

355   cholesterol - as assessed by FRAP (Fig. 4I and Suppl. Fig. 4A and see (*63*)). These results suggest

356   nanodomain assembly for the C16:0, C18:0, and notably C24:1$^{\Delta 15}$ GM1 lipids.

357   Thus overall, we found that the different GM1 species are sorted within live cells based on the

358   C14*-motif. These GM1 species were retained within the body of the sorting endosome for

359   maturation along the lysosomal pathway. And they exhibited dependence on membrane

360   cholesterol for their sorting and biophysical behaviors, consistent with an affinity for assembly

361   into membrane nanodomains (Fig. 5). In contrast, the GM1 species containing mono-

362   unsaturated acyl chains of 12 to 22 hydrocarbons atoms in length (thus lacking the C14*-motif)

14

363   did not display dependence on cholesterol for their membrane behaviors. And unlike the fully

364   saturated GM1 species, these GSLs entered endosome sorting tubules of the recycling and

365   retrograde endosome pathways.

366

Discussion

The results of our studies show that mammalian cells sort GM1 sphingolipids between endosomes and endosome sorting tubules, and within the plane of the PM, based on their ceramide acyl chain structure. This is explained by differential association with membrane cholesterol - likely mediated by lipid nanodomain formation (Fig. 2C and schematic in Fig.5). Lipid shape on its own (*55, 64-66*) cannot fully explain the selective entry of the different GM1 species into the narrow highly curved endosome sorting tubules, or their retention in the body of the sorting endosome. The differential sorting phenotypes observed were strictly dependent on membrane cholesterol content and ceramide structure, and the same structure-function relationships operated across multiple cell types known to vary in their overall membrane thickness, fluidity, and cholesterol content (our unpublished data and (*67-69*)). These results define a structural organizing principle for complex sphingolipid behavior in native heterogeneous and dynamic live cell membranes. The complex sphingolipids critically require more than 14 saturated hydrocarbons in the ceramide acyl chain extending from the C1-amide at the water-bilayer interface for optimal association with cholesterol. And this decisively affects their direction of endosome sorting. GSL species lacking these features escape the apparently active lysosomal sorting step and enter endosome sorting tubules of the recycling and retrograde pathways instead. These observations experimentally verify in live cells one of the underlying and fundamental biophysical processes hypothesized to shape lipid trafficking, membrane architecture, and cell function. It is possible the C14*-motif may also explain the differential sorting of ceramide-linked proteins in the secretory pathway recently observed in yeast (*41*).

In nature, the *cis*-double bond in the GM1 species containing mono-unsaturated acyl chains of 16 to 22 hydrocarbons atoms in length is positioned at carbon atom 9 or 13 (Δ^9 and Δ^{13}) extending from the amide linkage to sphingosine, and thus located within the outer leaflet of the membrane bilayer. Within this area, the "kink" in the acyl chain caused by unsaturation interferes with alignment against the flat and rigid sterol structure of cholesterol (*43, 70-74*). These GM1 species entered endosome sorting tubules of the recycling and retrograde

16

395   endosome pathways, and their trafficking was not dependent of cholesterol. On the other

396   hand, the GM1 species containing the very long mono-unsaturated acyl chains (C24:1$^{\Delta 15}$ and

397   C26:1$^{\Delta 17}$) trafficked to the lysosome - phenocopying the fully saturated GM1 species even

398   though they also contained a *cis*-double bond "kink" in their ceramide. Here, the structural

399   analysis was most informative. The *cis*-double bond in these native acyl chains is located at Δ^{15}

400   or Δ^{17}, below the stretch of 14 saturated hydrocarbons from the amide linkage at the

401   membrane surface (*44, 70*), and below the expected interface with the sterol rings of

402   cholesterol (*43*). Thus, the acyl chains of these GM1 species recapitulated exactly the minimal

403   saturated hydrocarbon chain length that we found required for endosome sorting of the GSLs

404   to the lysosome. Notably, the membrane behavior of these very long unsaturated GM1 species

405   in live cells was strictly dependent on membrane cholesterol, analogous to the fully saturated

406   acyl chain GM1 species. Two species GM1 C14:0 and GM1 C22:1$^{\Delta 13}$ had intermediate

407   phenotypes for cholesterol dependence - these ceramides have acyl chain lengths that border

408   on the minimal C14*-motif required for functional association with cholesterol.

409   The strong dependence on cholesterol for the membrane behaviors of the saturated and very

410   long chain unsaturated GM1 species conforms to central tenants of the lipid raft hypothesis.

411   The raft hypothesis posits that certain lipids and cholesterol phase separate into ordered and

412   tightly packed domains, mediated through hydrogen bonding and van der Waals forces, and

413   shaped by cellular protein scaffolds, including by bonding to the cortical actin cytoskeleton (*18,*

414   *20, 75*). For the saturated and very long chain unsaturated GSLs, we find evidence for their

415   assembly into membrane nanodomains: perhaps best evidenced by the segregation of these

416   GM1 species in separate regions of artificially enlarged early endosomes. Our results are

417   consistent with another structural factor implicated in nanodomain assembly for GPI-anchored

418   proteins and recently for GM1 ((*76*) and our unpublished results, Arumugam et al.): the need

419   for direct extension of outer membrane lipids into the inner-membrane lipid leaflet for

420   assembly with phosphatidyserine and the cortical actin cytoskeleton. In those studies, we found

421   that the ceramide C14*-motif was required for features of nanodomains with linkage to the

422   cortical cytoskeleton as assessed by fluorescence correlation microscopy. Nanodomain

423   formation, and GM1 trafficking, may also be affected by extracellular factors that induce lipid

424   clustering (*14*), as we found for CTxB (*40*).

425   The structural diversity of ceramide moieties comprising the complex sphingolipids that occur

426   in nature is perhaps best defined for sphingomyelin, which is the most highly prevalent complex

427   sphingolipid, and thus most easily and reproducibly studied. In our hands, and in the cell-type

428   examined, we found that the predominant ceramide moieties in sphingomyelin contained

429   C18:0, C18:1$^{\Delta 9}$, C24:0, and C24:1$^{\Delta 15}$ acyl chains. This, and published lipidomic analyses of

430   sphingomyelin in other cell types, suggest the evolution of two 'bi-modal' structure-function

431   distributions for the complex sphingolipids: one between long and very long ceramide acyl

432   chains as proposed before [(*46*)61-64], and the other between saturation and unsaturation as

433   we find here. Experimentally, these two bi-modal distributions were evident in our structure-

434   function studies on GM1. In the case of unsaturation, the different membrane behaviors were

435   most readily apparent for the saturated GM1 C18:0 and the unsaturated C18:1 species. But this

436   dichotomy of saturation and unsaturation was not absolute - it also depended on acyl chain

437   length. In the case of GM1 species with very long C24:0, and C24:1$^{\Delta 15}$ acyl chains, for example,

438   these GSLs behaved mostly in the same way - even though one was saturated and the other

439   was not. Thus, acyl chain length in the native complex sphingolipids appears to over-ride the

440   functional impact of unsaturation, as long as the *cis*-double bond is positioned below a stretch

441   of saturated hydrocarbons of sufficient length (beyond the C14*-motif). The long and very long

442   acyl chains may also enable interdigitation with the contralateral lipid leaflet (*77-79*). Lipid

443   shape, on its own, does not appear to act decisively for entry of the GSLs into endosome sorting

444   tubules, or for their endosomal sorting – contrary to the impact of acyl chain unsaturation on L_d

445   and L_o phase separation and nanodomain assembly in GPMVs.

446   We also note that some very long unsaturated acyl chain GM1 species, typified by GM1

447   C24:1$^{\Delta 15}$, exhibited graded membrane behaviors that bridged the dichotomy between

448   saturation and unsaturation seen in the GM1 C18:0 and C18:1 pair. These very long acyl chain

449   GSLs sorted predominantly to the lysosome, but a significant portion sorted also into the

450   recycling pathway - in contrast to their fully saturated counterparts. In addition, GM1 C24:1$^{\Delta 15}$

18

451   had a restricted but still higher degree of apparent endocytic uptake compared to its fully

452   saturated counterpart. Thus, the very long chain unsaturated GSLs appear to occupy a

453   functionally intermediate space. They may have been evolutionarily conserved according to

454   their graded membrane behaviors in membrane sorting so as to more readily enable

455   differential responses to small alterations in membrane structure and composition caused by

456   cell stress, cell differentiation, or even to the normal dynamic changes in membrane content

457   produced by trafficking from one organelle to another in cells at steady state (*80*).

458   In summary, our studies show that the membrane behaviors of the complex sphingolipids are

459   defined by two general rules of ceramide structure - hydrocarbon acyl chain length and

460   unsaturation. This includes the position of the *cis*-double bond with respect to the outer leaflet

461   of the membrane lipid bilayer and how acyl chain length and saturation affect the ability of

462   GSLs to associate with cholesterol and possibly to form nanodomains. These basic structural

463   principles are of general importance to cell and tissue biology, as the segregation and behavior

464   of lipids has fundamental physiological consequences for membrane organization and the

465   plasticity required to accommodate the diversity of membrane dynamics underlying cell

466   functions.

467

468 **Material and Methods**

469 Dimethylformamide (DMF), dimethylsulfoxide (DMSO), methyl-β-cyclodextrin (MβCD), soluble

470 cholesterol complexed to MβCD, defatted bovine serum albumin (dfBSA), fetal bovine serum

471 (FBS), fetal bovine serum depleted of HDL (HDL-), Simvastatin (statin), T0901317 (T09),

472 U18666A (U18) and filipin III (filipin) were purchased from Sigma Aldrich (St. Louis, MO).

473 Dulbecco's modified Eagle's medium (DMEM) with or without phenol red, OptiMEM®,

474 Lipofectamine® 2000, Laurdan (6-Dodecanoyl-2-Dimethylaminophthalene), *FAST*DiI™ DiI$^{\Delta 9,12}$-

475 C$_{18}$(3), ClO$_4$ (1,1'-Dilinoleyl-3,3,3',3'-Tetramethylindocarbocyanine Perchlorate), *FAST*Dio™

476 DiO$^{\Delta 9,12}$-C$_{18}$(3), ClO$_4$ (3,3' Dilinoleyloxacarbocyanine Perchlorate)), various AlexaFluor™ (- 405, -

477 488, - 568, or - 647 nm) or pHrodo™Fluor -NHS esters and –azide dyes, AlexaFluor™ and

478 pHrodo™Fluor conjugates, Dextran Pacific Blue™ (3000 MW) and LysoTracker™ were purchased

479 from Thermo Fisher Scientific (Waltham, MA).

480 **Cell culture**

481 Human epithelial A431, HT29, CaCo and Hela cells, as well as HEK293T cells were originally

482 purchased from the American Tissue Culture Collection (ATCC, VA). Cells were maintained in

483 Dulbecco's modified Eagle's medium (DMEM) containing 10% FBS with penicillin and

484 streptomycin. Cultures were split two days prior to experiment to achieve the desired

485 confluency state. The CRISPR-Cas9 SVGA Rab5-GFP cell line was maintained in MEM containing

486 10% FBS.

487 For cholesterol addition and/or depletion assays, cells were cultured for 24 h in [50 – 100 nM]

488 T0901317, or for 12 h in [1 -2 μg/ml] U18666A in full medium and for 24 h for [10 μM]

489 simvastatin in serum depleted of HDL. Soluble cholesterol complexed to MβCD [120 μg/ml] was

490 given in full media for 30 min or the indicated time. Efficacy of treatment was determined by

491 fixing treated cells in 4 % paraformaldehyde for 1 h and subsequently staining cells with [0.05

492 mg/ml] filipin III to determine plasma membrane cholesterol contents by fluorescence. Plasma

493 membrane fluorescence intensity was measured using the Fiji (ImageJ, National Institutes of

494   Health, Bethesda, MD, USA) segmented line tool to outline plasma membrane and mean grey

495   values were obtained.

496   To obtain enlarged Rab5 early endosomes, A431 cells were transfected using Lipofectamine®

497   2000 and OptiMEM® transfection method according to manufacturer's instructions and 500 –

498   1000 ng of the Addgene plasmids (#28046, #35138).

Generation of CRISPR-Cas9 KO cell lines

499

500   CRISPR-Cas9 KO cell lines were generated using Addgene plasmid lentiCas9-Blast (#52962) for

501   stable integration of Cas9 endonuclease and guide sequences were cloned into Addgene

502   plasmid lentiGuide-Puro (#52963) against ceramide synthase 1, 2 and 5 (CerS1, 2 and 5), UDP-

503   glucosyl-ceramide glucosyltransferase (UGCG), and serine palmityl transferase 2 (SPTLC-2) (see

504   Table 1). Plasmids were verified by sequencing using IDT technologies (Coralville, IA). [1.5 µg]

505   plasmids were co-transfected with packaging plasmids pVSVg [0.5 µg] and psPAX2 [1 µg]

506   Addgene plasmids #8454, #12260 in the presence of polyethylenimine (PEI) into HEK293T cells

507   for lentivirus production. 48 h post transfection virus was harvested and mixed with respective

508   cell line. Clones were selected for 7 days on [10 µg/ml] Blasticidin and/or [1 µg/ml] Puromycin.

509   KO cell lines were tested for CTxB binding by FACS and low binding population was sorted.

510   Cell lines carrying an ER version of Split-GFP were constructed according to Luong et al. (*60*) and

511   selected on Hygromycin [50 µg/ml] for 7 days.

Synthesis of peptide and fluorophore-labeled GM1 species

512

513   Gangliosides of various fatty acid species were supplied by Prof. Sandro Sonnino (U. Milan,

514   Italy). Reporter peptide containing modified functional residues were custom synthesized by

515   New England Peptide (Gardner, MA) as all-D peptides with the following amino acid sequence:

516   propargylglycine-k(ε-biotinoyl)(ds)g(dy)g(dr)g(ds)g-(kaoa)-amine. Synthesis of peptide-lipid and

517   fluorophore labeled conjugates was accomplished with minor modifications according to

518   Garcia-Castillo et al., te Welscher *et al.* and Chinnapen et al. (*40, 47, 48*).

21

519   In a typical 2 ml reaction, 2 mg (approximately 1300 nmoles) of ganglioside was oxidized with

520   sodium periodate (13 mmoles) in oxidation buffer (100 mM sodium acetate pH 5.5, 150 mM

521   NaCl) for 30 min on ice. The reaction was quenched by addition of glycerol (5% final) and

522   desalted using a Bond Elut SepPak C18 cartridge (Agilent, MA). Methanol was used to elute

523   oxidized GM1 species from the column and was removed by Speed Vac concentration (Savant).

524   The oxidized product was then reconstituted in 2 ml PBS pH 6.9 in the presence of 10% DMF

525   and reacted with 2700 nmoles of aminooxy-containing peptide in the presence of 10 mM

526   aniline (Dirksen and Dawson, 2008). The reaction was incubated for 20 h at room temperature

527   with mixing on a nutator. The precipitate was separated from the solution by centrifugation,

528   and then resuspended in 400 µl 50% isopropanol/water after brief sonication. PBS pH 6.9 was

529   added (200 µL) along with 4.8 mmoles of sodium cyanoborohydride and incubated for 3 h to

530   reduce the oxime bond. Lipid-peptide conjugates were purified by semi-preparative HPLC, and

531   confirmed by either MALDI-TOF (AB Voyager), or ESI LC-MS (Agilent, MA).

532   Peptides were labeled with Alexa fluorophore via copper mediated Click chemistry. 320 mM

533   peptide-lipid fusions containing an N-terminal alkyne residue (propargylglycine) were reacted

534   with equimolar concentrations of AlexaFluor™ -azide under the following conditions: 50 mM

535   Tris-Cl, 5 mM copper (II) sulfate, 100 mM sodium ascorbate, 37 mM (Tris[(1-benzyl-1H-1,2,3-

536   triazol-4-yl)methyl]amine, TBTA in DMSO/t-butanol 1:4) 1 mM (Tris(2-carboxyethyl) phosphine

537   hydrochloride, TCEP – Sigma) for 16 h at room temperature on a nutator. Products were

538   purified by HPLC and confirmed by mass spectrometry. Products were lyophilized and stored at

539   - 20˚C or - 80˚C for long term storage.

540   Working stock solutions were prepared in 33% DMF/ddH20.

541   Alternatively, fatty acyl variant gangliosides were fluorophore labeled directly via the

542   oligosaccharide head group following the oxidation of the ganglioside. The oxidized

543   gangliosides were resuspended in phosphate buffered saline pH 7.4 (PBS) and reacted with 1

544   mole AlexaFluor™-azide (Invitrogen, OR) for 16 h. Ten moles sodium cyanoborohydride was

545   added to the reaction for 15 minutes and the mixture was desalted on Bond-Elute cartridges.

546   Ganglioside-fluorophore conjugates resulted in a different mobility band visible by TLC and

547   were purified using preparative-TLC plates. Extraction from silica scrapings was performed, and

548   the conjugates further purified by reversed phase C18 cartridges.

549   **FACS based assay for lipid recycling, retrograde and lysosomal trafficking**

550   Cell lines were plated on 96 well plates and grown to 70% confluency (unless otherwise stated)

551   with or without treatment. Cells were washed and equilibrated with serum-free DMEM (no

552   phenol red) for 5 min at 37˚C. GM1 species were diluted to four different concentrations of the

553   respective peptide-labeled GM1 species in serum-free DMEM with equimolar ratio of dfBSA

554   (1:1 lipid:dfBSA). Lipids were loaded for 10 min at 37˚C and washed of in serum-free DMEM (no

555   phenol red). To measure the amount of 'loaded' GM1, cells were trypsinized for 5 min at 37˚C,

556   then chilled to 4˚C and stained with respective streptavidin-AlexaFluor™ (1:2500, 2 mg/ml) in

557   PBS containing 5% BSA for 15 min/4˚C. Unbound streptavidin was washed off twice with PBS

558   containing 5% FBS and cells were FACS analyzed immediately, using a FACS Canto II (BD,

559   Biosciences, NJ). Lipid+ gate was determined against streptavidin stained control cells, not

560   loaded with GM1. The percentage of positive cells and their median fluorescence were

561   recorded. To compare the recycling efficiency between the different GM1 variants, the

562   respective concentrations resulting in equal median fluorescence or equal % of cells for the

563   'load' were chosen. To obtain 'chase' samples, the lipid was washed off and cells were

564   subsequently incubated for 3 h in DMEM containing 5% FBS in the presence of Dextran-Fluor

565   (500 µg/ml) and transferrin-AlexaFluor™ (1 µg/ml). Cells were then washed and trypsinized and

566   stained with streptavidin-AlexaFluor™ as described above. To compare recycling rates between

567   different treatments, recycling rates (median fluorescence) for non-treated or WT cells were

568   normalized to 1 and fold change difference to treated samples calculated.

569   To determine retrograde trafficking of CTxB-SplitGFP, native (non-peptide labeled) GM1 species

570   were loaded as above into either Hela cells or an A431 CRISPR-Cas9 UGCG-KO cell line. 'Load'

571   amount of lipid was determined using 5nM fluorescently labeled CTxB instead of streptavidin as

572   described above. 'Chase' samples were incubated in the presence of 10 nM CTxB-SplitGFP for

573   the indicated amount of time in DMEM containing 5% FBS. For retrograde trafficking in CRISPR-

23

574 Cas9 KO cell lines, cell surface GM1 amount was determined using 5nM fluorescently labeled

575 CTxB as described above and CTxB-SplitGFP values were normalized to cell surface GM1.

576 To measure lysosomal trafficking of GM1-CTxB complex, pH sensitive CTxB-pHrodo™ was used.

577 Cells were chilled to 4°C and stained using 5 nM CTxB-pHrodo™ in PBS containing 5% BSA.

578 Unbound CTxB was washed off and cells were incubated for the indicated amount of time at

579 37°C in in DMEM containing 5% FBS. Cell surface GM1 was determined using 5nM fluorescently

580 labeled CTxB as described above and CTxB-pHrodo™ values were normalized to cell surface

581 GM1.

582 Two biological replicates per assay were performed and a total of N = 10,000-20,000 single cells

583 recorded per treatment for all FACS based assays.

Lysosomal trafficking of EGF receptor and LDL receptor

585 Cells were grown as described above. To determine the lysosomal fraction of different

586 membrane protein receptors, cells were loaded with their respective ligands at (2 - 5 µg/ml),

587 labeled either as pH sensitive (phrodo™, FITC) or pH resistant (AlexaFluor™/Bodipy for LDL).

588 'Load' was determined by incubating pre-chilled cells for 10 min at 4°C with pH resistant ligand.

589 Cells were subsequent washed in PBS and detached using Cell Dissociation Buffer (Gibco).

590 Lysosomal fraction was determined by loading cells with pH sensitive ligand as above; after

591 washing off unbound ligand, cells were moved to 37°C for 2 h in the presence of fluorescent

592 dextran to normalize endocytosis rates. Cells were trypsinized and subsequently analyzed by

593 FACS.

Lipid loading, imaging and quantification for Airyscan or lattice lightsheet imaging

595 Cell lines were plated on either 35 mm MatTek petri dishes (Ashland, MA) containing glass

596 bottom for Airyscan confocal microscopy or on 3 mm cover slips for Lattice Lightsheet

597 microscopy and grown to 70 % confluency with or without treatment. Fluorescent GM1 variants

598 were added as described for the FACS based assays for lipid recycling unless otherwise noted.

599 To determine subcellular location, lipids were allowed to traffic for the indicated amount of

600   time at 37˚C in the presence of fluorescent transferrin (1 μg/ml) and lysoTracker™ (2 nM) or

601   dextran (1 mg/ml) to demarcate the respective organelles. Sorting endosomes were defined as

602   vesicles containing lipid as well as transferrin and dextran. Sorting endosomal tubules were

603   defined by presence of transferrin emerging from triple positive vesicles.

604   For lactose and sucrose addition experiments A431 cells were incubated for 30 min in the

605   presence of 100 mM lactose or sucrose prior/during and after GM1 loading.

606   Airyscan imaging was performed using Zeiss LSM 880 microscope with Airyscan detector and

607   Plan-Apochromat 63x oil immersion objective with NA = 1.4. Airyscan processing was

608   performed using the Zeiss ZenBlack software.

609   Quantification of GM1 in recycling endosomal tubules:

610   Region of interest (ROI) was determined, containing approximately 3 - 6 triple positive vesicles

611   and the ROI was thresholded using image quantification software ImageJ (Otsu). GM1

612   presence/absence (1/0) within transferrin positive tubules was recorded and % for the ROI

613   calculated.

614   Tubule over vesicle fluorescence quantification:

615   For GM1 C14:0 and C22:1$^{\Delta 13}$ as well as for samples treated with cholesterol lowering molecules,

616   or cholesterol addition, fluorescence grey values for the vesicle and tubule were recorded,

617   background fluorescence was subtracted and a ratio was determined by dividing the mean grey

618   value obtained for the tubule by the mean grey value obtained for the vesicle (Fig. 1H). The

619   same analysis was performed for Fig. 2G and Suppl. Fig. 4D.

620   Quantification of endocytic rates:

621   Endocytic rates were assayed using CRISPR-Cas9 modified SVGA cell line containing an

622   endogenous, RAB5-EGFP variant (*81*). GM1 variants were loaded as described above, washed

623   off and immediately transferred to the microscope. Cells were imaged for approx. 5 min each.

624 Vesicles were counted using ImageJ software and quantification was based on at least 5
625 biological replicates.

626 GM1 - Tfn co-localization in Rab5 enlarged early endosomes:

627 Using Fiji segmented line tool Rab5 early endosomes were traced using Rab5 fluorescence as
628 marker and mean grey fluorescence intensity profiles of GM1 variants and Tfn were exported
629 into GraphPad Prism. Pearson's correlation coefficient was calculated between different GM1
630 or Rab5 fluorescence profiles against Tfn fluorescence profile.

631 **Fluorescence recovery after bleaching (FRAP)**

632 Cell lines were plated on 35 mm MatTek petri dishes containing glass bottom 48 h prior to
633 experiments and treated as described above. GM1 lipids were incorporated into plasma
634 membranes as described above.

635 Cells were immediately transferred into preheated chamber for bleaching using the following
636 settings: 80 – 100 % laser intensity, pixel dwell time of approx. 170 μsec, membrane
637 fluorescence was bleached to about 20 - 40% of the original fluorescence intensity. Three ROIs
638 of similar size were chosen, one background ROI (ROI_{bg}) and two ROIs within the PM of a given
639 cells, with one of the latter being bleached (ROI_b), while the other served as reference
640 photobleaching control (ROI_{nb}). To establish the baseline, three – five frames were collected
641 before the bleaching event and to capture the recovery, at least fifteen frames were acquired
642 every 150 - 300 msec for a total time of approx. 10 sec post bleaching event.

643 FRAP curves were determined using the following formulas with pb = pre bleached fluorescence
644 (*82*):

645 $(1) \; Bleached \; Fraction(t) = 1 - [\frac{(ROI_b(t) - ROI_{bg})}{(ROI_{nb}(t) - ROI_{bg})} * \frac{(pbROI_{nb} - pbROI_{bg})}{(pbROI_b - ROI_{bg})}]$

646   (2)

647    $Fluorescence\ Recovery =$

648    $Bleached\ Fraction(t_{max}) - Bleached\ Fraction(t_{right\ after\ bleach})$

649   (3) $Mobile\ Fraction = \dfrac{Fluorescence\ Recovery}{Bleached\ Fraction(t_{right\ after\ bleach})}$

650   **GPMV generation**

651   Cells were seeded two days prior to assay on 12 well plates to reach desired confluency. Native

652   or fluorescently labeled GM1 species were added as described above, and a phase marker

653   (*FAST*DiO™ and *FAST*DiL™, 0.5 mg/ml − 1. 1:1000 in PBS) was added for 10 min. Phase marker

654   was washed off three times using PBS, then cells were equilibrated by washing twice in GPMV

655   buffer (50 mM Tris, pH = 8, 150 mM NaCl, 50 mM $CaCl_2$). Vesiculation was achieved according

656   to (*50*) by using 2 mM DTT and 0.07 % PFA in GPMV buffer and cells were incubated for 1-3 h at

657   37˚C (depending on the cell type). Supernatant containing GPMV vesicles were harvested and

658   sedimented 5 min/ 500 g. Vesicles were chilled to 10˚C and imaged. L_d phase was determined

659   by the phase marker and L_o partitioning coefficient (ordered phase partitioning coefficient = I_{lo})

660   was obtained using the following formula: $K_{raft} = I_{Lo}/I_{Ld}$. A $K_{lo} > 1$ indicates ordered phase

661   preference.

662   For membrane fluidity analysis, GPMVs were harvested from respective cells and/or treatments

663   as above and subsequently stained using [0.5 µM] laurdan for 3 h at RT. Dye was washed off

664   twice and vesicles were chilled to 10˚C prior to imaging. Imaging was achieved by using spectral

665   imaging with confocal microscope Zeiss LSM 880 using Plan-Apochromat 63x oil immersion

666   objective (NA 1.4). C-laurdan was excited at 405 nm and the emission was collected with a

667   multichannel spectral detector (PMT) in the range 430 - 450 nm and 480 - 500 nm

668   simultaneously. The polarity index, generalized polarization (GP) was calculated according to

669   Steinkuehler *et al.* (*68*) using the following formula: $GP = (I_{440} - I_{490})/(I_{440} + I_{490})$ where I_{440} and

670   I_{490} are the fluorescence intensities at 440 nm and 490 nm, respectively.

671

Lipid extraction and Lipidomic profiling of A431 WT and CRISPR-Cas9 KO cell lines

500,000 cells per biological/technical replicate were washed twice with PBS and then 0.25 x PBS to remove media components and transferred into glass vials. Cells were then pelleted to remove remaining supernatant and flash frozen in liquid nitrogen and pellet was subsequently lyophilized. Lipid extraction and lipidomic profiling was performed according to Liaw et al. and Kumar et al. (*83, 84*). In brief, the lyophilized pellet was homogenized in 1 ml ddH$_2$O, subsequently 2.2 ml methanol and 0.9 ml dichlormethane was added. Suspension was incubated o/N at -20C, before 20 µl Avanti Splash mix was added, mixture was vortexed and incubated for 10 min at RT. Then 1 ml ddH$_2$O, 0.9 ml dichloromethane and 0.5 ml methanol were added. Solution was centrifuged at 1200 rpm for 10 min and lower phase collected into fresh glass tube. 2 ml dichloromethane were added to the aqueous phase to extract any remaining lipids, mixture was centrifuged as above and the organic phase was pooled with the first one.

Solvent was evaporated in Genevac.

Unbiased MS/MSALL shotgun lipidomic profiling was performed on Sciex 5600 TripleTOF mass spectrometer.

Software and Statistical analysis

Imaging data was analyzed using either Zeiss ZENblack, Fiji or Aiviva 9 (Drvision Technologies, Bellevue, WA) software. Lattice lightsheet data obtained at the Janelia Farms Advanced Imaging center (AIC), deskewed and decovoluted using customized Matlab™ software.

Schematic Model in Fig. 1A was drawn using BioRender.

Mean grey fluorescent values of microscopy experiments or mean fluorescence data obtained from FACS experiments was transferred to GraphPad Prism software (San Diego, CA) for graphing and statistical analysis. Statistically significant difference between treatments was tested by One-way ANOVA with Tukey's multiple comparison; alternatively unpaired t-test was applied when indicated with

698   n.s. p > 0.05, *p < 0.05, **p < 0.01 ***p < 0.001 and ****p < 0.0001.

699   **Table 1**

700   CRISPR KO guide sequences

701   Guide sequences were used from AVANA sgGuide library (*85*).

Gene	sgGuide sequence
SPTLC-2	ACAACTATCTTGGATTTGCA
UGCG	ACAACTATCTTGGATTTGCA
CerS1	AGCGCTCTCGGGCATCTTGG
	GCTTCCCTGGAGCAGGTAGG
	GCAGCCGCCTACCTGCTCCA
	TACGCGCAGCTAGTGCAGC
CerS2	GCTGCCTGTGAACTTGACCT
	TTCTTCATGTCATAGAACCA
	GGTCAGGTAGAAATGTTCCA
	GTAAAATGTGAATCTCCAGC
CerS5	GTATCCTGATAAGAAAAGGC
	TGATGAAACCAAGACCCAAG
	ATGCCAATACAGAGTGCACA
	ATAAAATGTGAATCTCCACC

702

29

References

1. M. Koval, R. E. Pagano, Intracellular transport and metabolism of sphingomyelin. *Biochimica et biophysica acta* **1082**, 113 (Mar 12, 1991).
2. G. van Meer, K. Simons, Viruses budding from either the apical or the basolateral plasma membrane domain of MDCK cells have unique phospholipid compositions. *The EMBO journal* **1**, 847 (1982/07/01, 1982).
3. B. Ramstedt, J. P. Slotte, Membrane properties of sphingomyelins. *FEBS Lett* **531**, 33 (Oct 30, 2002).
4. S. Chiantia, E. London, in *Sphingolipids: Basic Science and Drug Development,* E. Gulbins, I. Petrache, Eds. (Springer Vienna, Vienna, 2013), pp. 33-55.
5. D. A. Brown, E. London, Structure and origin of ordered lipid domains in biological membranes. *J Membr Biol* **164**, 103 (Jul 15, 1998).
6. E. London, How principles of domain formation in model membranes may explain ambiguities concerning lipid raft formation in cells. *Bba-Mol Cell Res* **1746**, 203 (Dec 30, 2005).
7. D. Goswami *et al.*, Nanoclusters of GPI-anchored proteins are formed by cortical actin-driven activity. *Cell* **135**, 1085 (Dec 12, 2008).
8. K. Gowrishankar *et al.*, Active remodeling of cortical actin regulates spatiotemporal organization of cell surface molecules. *Cell* **149**, 1353 (Jun 8, 2012).
9. A. Kusumi *et al.*, Membrane mechanisms for signal transduction: the coupling of the meso-scale raft domains to membrane-skeleton-induced compartments and dynamic protein complexes. *Seminars in cell & developmental biology* **23**, 126 (Apr, 2012).
10. C. A. Day, A. K. Kenworthy, Mechanisms underlying the confined diffusion of cholera toxin B-subunit in intact cell membranes. *PLoS One* **7**, e34923 (2012).
11. A. Fujita, J. Cheng, T. Fujimoto, Segregation of GM1 and GM3 clusters in the cell membrane depends on the intact actin cytoskeleton. *Biochimica et biophysica acta* **1791**, 388 (May, 2009).
12. L. Johannes, R. G. Parton, P. Bassereau, S. Mayor, Building endocytic pits without clathrin.
13. L. J. Pike, Lipid rafts: heterogeneity on the high seas. *The Biochemical journal* **378**, 281 (Mar 1, 2004).
14. L. Johannes, R. G. Parton, P. Bassereau, S. Mayor, Building endocytic pits without clathrin. *Nat Rev Mol Cell Biol* **16**, 311 (May, 2015).
15. D. Lingwood, K. Simons, Lipid rafts as a membrane-organizing principle. *Science* **327**, 46 (Jan 1, 2010).
16. K. Jacobson, P. Liu, B. C. Lagerholm, The Lateral Organization and Mobility of Plasma Membrane Components. *Cell* **177**, 806 (May 2, 2019).
17. K. Raghunathan, A. K. Kenworthy, Dynamic pattern generation in cell membranes: Current insights into membrane organization. *Biochim Biophys Acta Biomembr* **1860**, 2018 (Oct, 2018).
18. E. Sezgin, I. Levental, S. Mayor, C. Eggeling, The mystery of membrane organization: composition, regulation and roles of lipid rafts. *Nat Rev Mol Cell Biol* **18**, 361 (Jun, 2017).
19. K. Simons, J. L. Sampaio, Membrane organization and lipid rafts. *Cold Spring Harb Perspect Biol* **3**, a004697 (Oct 1, 2011).
20. K. Simons, G. van Meer, Lipid sorting in epithelial cells. *Biochemistry* **27**, 6197 (1988).
21. P. Varshney, V. Yadav, N. Saini, Lipid rafts in immune signalling: current progress and future perspective. *Immunology* **149**, 13 (Sep, 2016).
22. Y. Zhou, J. F. Hancock, Ras nanoclusters: Versatile lipid-based signaling platforms. *Biochimica et biophysica acta* **1853**, 841 (Apr, 2015).

748 23. M. F. Garcia-Parajo, A. Cambi, J. A. Torreno-Pina, N. Thompson, K. Jacobson, Nanoclustering as a
749   dominant feature of plasma membrane organization. *Journal of cell science* **127**, 4995 (2014).
750 24. J. Lippincott-Schwartz, R. D. Phair, Lipids and cholesterol as regulators of traffic in the
751   endomembrane system. *Annu Rev Biophys* **39**, 559 (2010).
752 25. G. H. Patterson *et al.*, Transport through the Golgi apparatus by rapid partitioning within a two-
753   phase membrane system. *Cell* **133**, 1055 (Jun 13, 2008).
754 26. Y. Deng, F. E. Rivera-Molina, D. K. Toomre, C. G. Burd, Sphingomyelin is sorted at the trans Golgi
755   network into a distinct class of secretory vesicle. *Proc Natl Acad Sci U S A* **113**, 6677 (Jun 14,
756   2016).
757 27. M. B. Stone, S. A. Shelby, M. F. Nunez, K. Wisser, S. L. Veatch, Protein sorting by lipid phase-like
758   domains supports emergent signaling function in B lymphocyte plasma membranes. *Elife* **6**,
759   e19891 (Feb 1, 2017).
760 28. W. I. Lencer, B. Tsai, The intracellular voyage of cholera toxin: going retro. *Trends in biochemical*
761   *sciences* **28**, 639 (Dec, 2003).
762 29. P. Cuatrecasas, Gangliosides and membrane receptors for cholera toxin. *Biochemistry* **12**, 3558
763   (Aug 28, 1973).
764 30. M. A. Campanero-Rhodes *et al.*, N-glycolyl GM1 ganglioside as a receptor for simian virus 40. *J*
765   *Virol* **81**, 12846 (Dec, 2007).
766 31. K. Sandvig, Shiga toxins. *Toxicon* **39**, 1629 (Nov, 2001).
767 32. M. Lorizate *et al.*, Comparative lipidomics analysis of HIV-1 particles and their producer cell
768   membrane in different cell lines. *Cell Microbiol* **15**, 292 (Feb, 2013).
769 33. W. Romer *et al.*, Shiga toxin induces tubular membrane invaginations for its uptake into cells.
770   *Nature* **450**, 670 (Nov 29, 2007).
771 34. R. Lakshminarayan *et al.*, Galectin-3 drives glycosphingolipid-dependent biogenesis of clathrin-
772   independent carriers. *Nat Cell Biol* **16**, 595 (Jun, 2014).
773 35. Y. A. Hannun, L. M. Obeid, Sphingolipids and their metabolism in physiology and disease. *Nat*
774   *Rev Mol Cell Biol* **19**, 175 (Mar, 2018).
775 36. A. H. Merrill, Jr., Sphingolipid and glycosphingolipid metabolic pathways in the era of
776   sphingolipidomics. *Chem Rev* **111**, 6387 (Oct 12, 2011).
777 37. W. W. Young, M. S. Lutz, W. A. Blackburn, Endogenous glycosphingolipids move to the cell
778   surface at a rate consistent with bulk flow estimates. *Journal of Biological Chemistry* **267**, 12011
779   (1992/06/15/, 1992).
780 38. G. van Meer, D. R. Voelker, G. W. Feigenson, Membrane lipids: where they are and how they
781   behave. *Nat Rev Mol Cell Biol* **9**, 112 (Feb, 2008).
782 39. D. E. Saslowsky *et al.*, Ganglioside GM1-mediated transcytosis of cholera toxin bypasses the
783   retrograde pathway and depends on the structure of the ceramide domain. *J Biol Chem* **288**,
784   25804 (Sep 6, 2013).
785 40. D. J. Chinnapen *et al.*, Lipid sorting by ceramide structure from plasma membrane to ER for the
786   cholera toxin receptor ganglioside GM1. *Developmental cell* **23**, 573 (Sep 11, 2012).
787 41. S. Rodriguez-Gallardo *et al.*, Ceramide chain length-dependent protein sorting into selective
788   endoplasmic reticulum exit sites. *Sci Adv* **6**, (Dec, 2020).
789 42. C. M. Paton, J. M. Ntambi, Biochemical and physiological function of stearoyl-CoA desaturase.
790   *American journal of physiology. Endocrinology and metabolism* **297**, E28 (Jul, 2009).
791 43. B. Ramstedt, J. P. Slotte, Interaction of cholesterol with sphingomyelins and acyl-chain-matched
792   phosphatidylcholines: a comparative study of the effect of the chain length. *Biophys J* **76**, 908
793   (Feb, 1999).
794 44. A. Kihara, Very long-chain fatty acids: elongation, physiology and related disorders. *Journal of*
795   *biochemistry* **152**, 387 (Nov, 2012).

796 45. S. Kavaliauskiene *et al.*, Cell density-induced changes in lipid composition and intracellular
797   trafficking. *Cellular and molecular life sciences : CMLS* **71**, 1097 (Mar, 2014).
798 46. R. L. Shaner *et al.*, Quantitative analysis of sphingolipids for lipidomics using triple quadrupole
799   and quadrupole linear ion trap mass spectrometers. *J Lipid Res* **50**, 1692 (Aug, 2009).
800 47. Y. M. te Welscher, D. J. Chinnapen, L. Kaoutzani, R. J. Mrsny, W. I. Lencer, Unsaturated
801   glycoceramides as molecular carriers for mucosal drug delivery of GLP-1. *J Control Release* **175**,
802   72 (Feb 10, 2014).
803 48. M. D. Garcia-Castillo *et al.*, Mucosal absorption of therapeutic peptides by harnessing the
804   endogenous sorting of glycosphingolipids. *Elife* **7**, e34469 (May 31, 2018).
805 49. S. L. Veatch, S. L. Keller, Separation of liquid phases in giant vesicles of ternary mixtures of
806   phospholipids and cholesterol. *Biophys J* **85**, 3074 (Nov, 2003).
807 50. E. Sezgin *et al.*, Elucidating membrane structure and protein behavior using giant plasma
808   membrane vesicles. *Nat Protoc* **7**, 1042 (May 3, 2012).
809 51. F. R. Maxfield, T. E. McGraw, Endocytic recycling. *Nat Rev Mol Cell Biol* **5**, 121 (Feb, 2004).
810 52. S. Mukherjee, R. N. Ghosh, F. R. Maxfield, Endocytosis. *Physiol Rev* **77**, 759 (Jul, 1997).
811 53. S. B. Kellie, B. Patel, J. Pierce, D. Critchley, Capping of cholera toxin - Ganglioside GM1 complexes
812   on mouse lymphocytes is accompanied by co-capping of alpha-actinin. *J. Cell Biol.* **97**, 447
813   (1983).
814 54. A. M. Kabbani, K. Raghunathan, W. I. Lencer, A. K. Kenworthy, C. V. Kelly, Structured clustering
815   of the glycosphingolipid GM1 is required for membrane curvature induced by cholera toxin.
816   *Proceedings Of The National Academy Of Sciences Of The United States Of America.* **117**, 14978
817   (Jun 30, 2020).
818 55. B. Sorre *et al.*, Curvature-driven lipid sorting needs proximity to a demixing point and is aided by
819   proteins. *Proc Natl Acad Sci U S A* **106**, 5622 (Apr 7, 2009).
820 56. B. N. Stillman *et al.*, Galectin-3 and galectin-1 bind distinct cell surface glycoprotein receptors to
821   induce T cell death. *Journal of immunology* **176**, 778 (Jan 15, 2006).
822 57. S. Mayor, J. F. Presley, F. R. Maxfield, Sorting of membrane components from endosomes and
823   subsequent recycling to the cell surface occurs by a bulk flow process. *J Cell Biol* **121**, 1257 (Jun,
824   1993).
825 58. A. A. Wolf *et al.*, Attenuated Endocytosis and Toxicity of a Mutant Cholera Toxin with Decreased
826   Ability to Cluster Gm1. *Infect Immun* **76**, 1476 (Jan 22, 2008).
827 59. K. Raghunathan *et al.*, Glycolipid Crosslinking Is Required for Cholera Toxin to Partition Into and
828   Stabilize Ordered Domains. *Biophys J*, (Nov 30, 2016).
829 60. P. Luong *et al.*, A quantitative single-cell assay for retrograde membrane traffic enables rapid
830   detection of defects in cellular organization. *Molecular biology of the cell* **31**, 511 (2020).
831 61. J. W. Park, W. J. Park, A. H. Futerman, Ceramide synthases as potential targets for therapeutic
832   intervention in human diseases. *Biochimica et biophysica acta* **1841**, 671 (May, 2014).
833 62. K. M. Spillane *et al.*, High-speed single-particle tracking of GM1 in model membranes reveals
834   anomalous diffusion due to interleaflet coupling and molecular pinning. *Nano Lett* **14**, 5390 (Sep
835   10, 2014).
836 63. J. S. Goodwin, K. R. Drake, C. L. Remmert, A. K. Kenworthy, Ras diffusion is sensitive to plasma
837   membrane viscosity. *Biophys J* **89**, 1398 (Aug, 2005).
838 64. A. Roux *et al.*, Role of curvature and phase transition in lipid sorting and fission of membrane
839   tubules. *The EMBO journal* **24**, 1537 (Apr 20, 2005).
840 65. T. Baumgart, S. T. Hess, W. W. Webb, Imaging coexisting fluid domains in biomembrane models
841   coupling curvature and line tension. *Nature* **425**, 821 (Oct 23, 2003).
842 66. S. Mukherjee, T. T. Soe, F. R. Maxfield, Endocytic sorting of lipid analogues differing solely in the
843   chemistry of their hydrophobic tails. *J Cell Biol* **144**, 1271 (Mar 22, 1999).

844 67.   P. Noutsi, E. Gratton, S. Chaieb, Assessment of Membrane Fluidity Fluctuations during Cellular
845   Development Reveals Time and Cell Type Specificity. *PLoS One* **11**, e0158313 (2016).
846 68.   J. Steinkuhler, E. Sezgin, I. Urbancic, C. Eggeling, R. Dimova, Mechanical properties of plasma
847   membrane vesicles correlate with lipid order, viscosity and cell density. *Commun Biol* **2**, 337
848   (2019/09/13, 2019).
849 69.   M. Hao, S. Mukherjee, Y. Sun, F. R. Maxfield, Effects of cholesterol depletion and increased lipid
850   unsaturation on the properties of endocytic membranes. *The Journal of biological chemistry*
851   **279**, 14171 (Apr 2, 2004).
852 70.   A. Kihara, Very long-chain fatty acids: elongation, physiology and related disorders.
853 71.   M. L. Fanani, B. Maggio, The many faces (and phases) of ceramide and sphingomyelin I - single
854   lipids. *Biophys Rev* **9**, 589 (Oct, 2017).
855 72.   M. L. Fanani, B. Maggio, The many faces (and phases) of ceramide and sphingomyelin II - binary
856   mixtures. *Biophys Rev* **9**, 601 (Oct, 2017).
857 73.   G. W. Stockton, I. C. Smith, A deuterium nuclear magnetic resonance study of the condensing
858   effect of cholesterol on egg phosphatidylcholine bilayer membranes. I. Perdeuterated fatty acid
859   probes. *Chem Phys Lipids* **17**, 251 (Oct, 1976).
860 74.   S. Jaikishan, A. Bjorkbom, J. P. Slotte, Sphingomyelin analogs with branched N-acyl chains: the
861   position of branching dramatically affects acyl chain order and sterol interactions in bilayer
862   membranes. *Biochimica et biophysica acta* **1798**, 1987 (Oct, 2010).
863 75.   K. Simons, W. L. Vaz, Model systems, lipid rafts, and cell membranes. *Annu Rev Biophys Biomol*
864   *Struct* **33**, 269 (2004/06/09, 2004).
865 76.   R. Raghupathy *et al.*, Transbilayer lipid interactions mediate nanoclustering of lipid-anchored
866   proteins. *Cell* **161**, 581 (Apr 23, 2015).
867 77.   T. Fujimoto, I. Parmryd, Interleaflet Coupling, Pinning, and Leaflet Asymmetry—Major Players in
868   Plasma Membrane Nanodomain Formation. *Frontiers in Cell and Developmental Biology* **4**, 155
869   (2017).
870 78.   T. Rog *et al.*, Interdigitation of long-chain sphingomyelin induces coupling of membrane leaflets
871   in a cholesterol dependent manner. *Biochimica et biophysica acta* **1858**, 281 (Feb, 2016).
872 79.   T. Skotland, K. Sandvig, The role of PS 18:0/18:1 in membrane function. *Nat Commun* **10**, 2752
873   (Jun 21, 2019).
874 80.   T. K. M. Nyholm *et al.*, Impact of Acyl Chain Mismatch on the Formation and Properties of
875   Sphingomyelin-Cholesterol Domains. *Biophys J* **117**, 1577 (Nov 5, 2019).
876 81.   Y. Y. Chou *et al.*, Identification and Characterization of a Novel Broad-Spectrum Virus Entry
877   Inhibitor. *J Virol* **90**, 4494 (May, 2016).
878 82.   M. Nissim-Rafinia, E. Meshorer, Photobleaching assays (FRAP & FLIP) to measure chromatin
879   protein dynamics in living embryonic stem cells. *Journal of visualized experiments : JoVE*, e2696
880   (Jun 29, 2011).
881 83.   L. Liaw *et al.*, Lipid Profiling of In Vitro Cell Models of Adipogenic Differentiation: Relationships
882   With Mouse Adipose Tissues. *J Cell Biochem* **117**, 2182 (Sep, 2016).
883 84.   N. Gajenthra Kumar *et al.*, Untargeted lipidomic analysis to broadly characterize the effects of
884   pathogenic and non-pathogenic staphylococci on mammalian lipids. *PLoS One* **13**, e0206606
885   (2018).
886 85.   J. G. Doench *et al.*, Optimized sgRNA design to maximize activity and minimize off-target effects
887   of CRISPR-Cas9. *Nat Biotechnol* **34**, 184 (Feb, 2016).
888

Acknowledgements

Author contributions

S.S.S and W.I.L. conceive study; S.S.S, R.T., W.I.L. designed experiments and resources; S.S.S, R.T. and K.K. performed experiments; S.S.S, R.T., and M.A. analyzed data. S.S.S. and W.I.L., wrote manuscript.
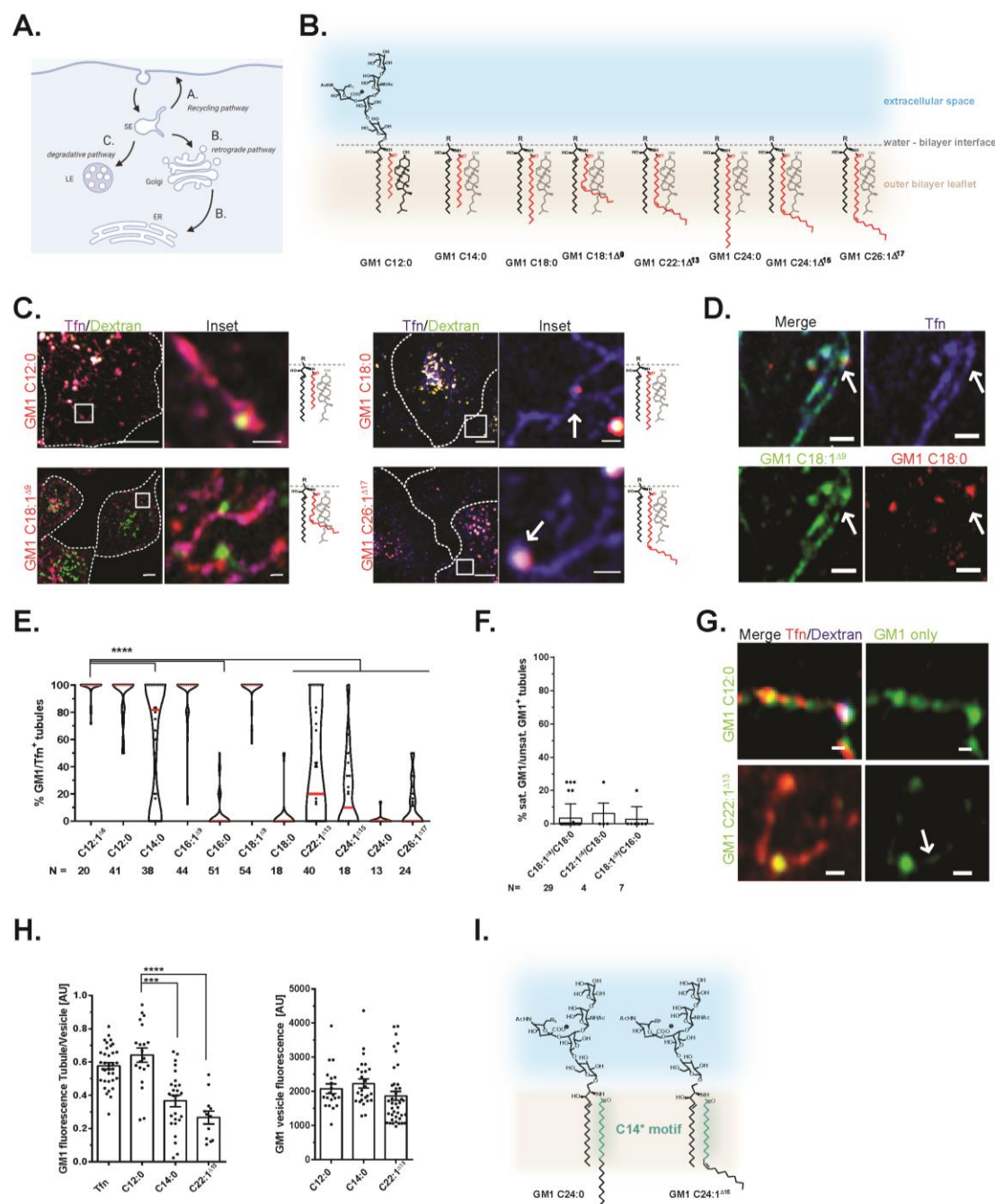
913　**Figures**

914

915　**Fig. 1. Ceramide structure-specific trafficking within the sorting endosome. (A)** Schematic of

916　endocytic pathways emerging from the sorting endosome (SE). Both the recycling and

917　retrograde pathways (marked A and B) require sorting into narrow endosomal tubules. Cargos

918　destined for degradation are retained within the sorting endosomal body for maturation to late

919   endosomes (LE) (marked C). **(B)** Library of GM1 species synthesized - acyl chains marked in red

920   and arbitrarily aligned against cholesterol to mark changes in structure. GM1 C12:1$^{\Delta6}$, C16:0 and

921   GM1 C16:1$^{\Delta9}$, species not shown. **(C)** Airyscan live cell imaging of recycling endosomal vesicles

922   in A431 epithelial cells. Scale bars = 5 and 0.5 µm respectively. **(D)** Same as panel C for cells

923   treated with GM1 C18:1$^{\Delta9}$ (green) and GM1 C18:0 (red). Scale bar = 1 µm. **(E)** Quantification of

924   GM1 presence in Tfn marked recycling endosomal tubules. Mean ± SEM, **** p = < 0.0001 by

925   one-way ANOVA and Tukey's multiple comparison using GM1 C12:0 as comparison. **(F)** Co-

926   localization of GM1 C18:0 or C16:0 with GM1 C18:1$^{\Delta9}$ or C12:1$^{\Delta6}$ species in recycling Tfn-positive

927   endosomal tubules. Quantification and statistics as in panel E. **(G)** Recycling tubules analyzed as

928   in Panel C using GM1 C22:1$^{\Delta13}$ and GM1 C12:0 species (green), Tfn (red). Scale bar = 0.5 µm. **(H)**

929   Left panel: Quantification of mean grey values of GM1 fluorescence in Tfn tubule normalized to

930   GM1 fluorescence in body of recycling endosomes for GM1 C12:0, C14:0 and C22:1 $^{\Delta13}$. Right

931   panel: Mean grey value of GM1 fluorescence in body of recycling endosome for the same GM1

932   species. Mean ± SEM. **** p = < 0.0001 against GM1 C12:0 by One-way ANOVA and Tukey's

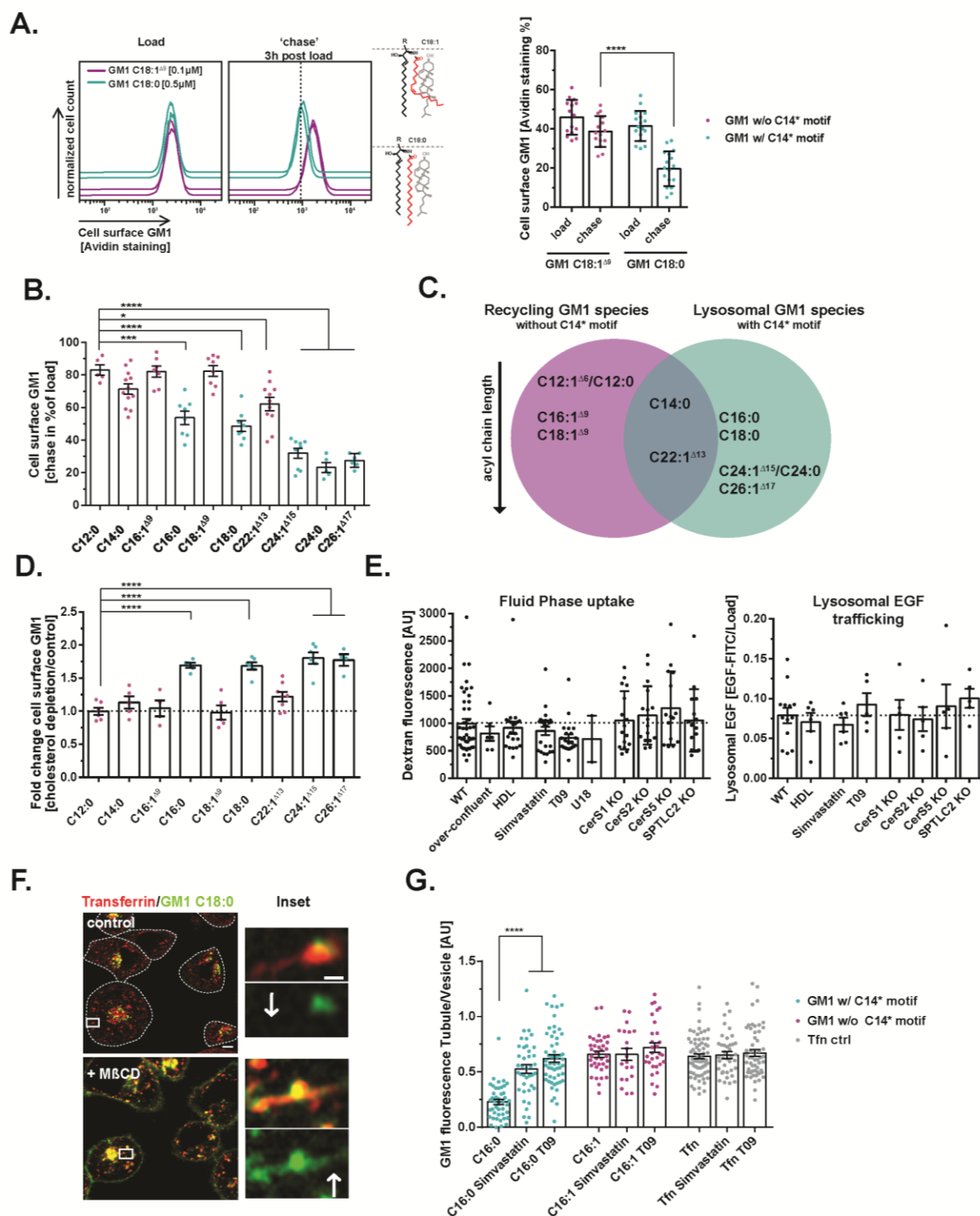933   multiple comparison. **(I)** GM1 C24:0 and GM1 C24:1$^{\Delta15}$, C14* motif in turquoise.

934

Fig. 2. C14* motif dictates differential sorting between the lysosomal and recycling pathways.

936 **(A)** PM concentrations of GM1 C18:0 (turquoise, with C14* motif) and GM1 C18:1$^{\Delta9}$ (magenta,

937 without C14* motif) as assessed by FACS using AlexaFluor™-labeled streptavidin before and

938 after 3 h chase. Mean ± SEM (right panel), each dot equals 2 biological replicates measuring

939 20,000 cells each. **** p = < 0.0001 by unpaired t-test. **(B)** Plasma membrane recycling as in

940 panel A for the GM1 structural library (GM1 species with C14* motif in turquoise, GM1 species

941 without C14* motif in magenta). Mean ± SEM. One-way ANOVA and Tukey's multiple

942 comparison. **(C)** Venn diagram for ceramide acyl chain structure dependent GM1 sorting in the

943 endosomal system. Recycling GM1 species, without C14* motif are in magenta and GM1

944 species entering the lysosomal pathway, containing the C14* motif are in turquoise. **(D)** Change

945 in recycling rates under mildly cholesterol depleting conditions as indicated. **** p = < 0.0001

946 by One-way ANOVA and Tukey's multiple comparison. **(E)** Fluid phase uptake (left) and

947 lysosomal trafficking (right) measured by FACS in A431 cells depleted or not of cholesterol as

948 indicated. No differences were observed as measured by One-way ANOVA and Tukey's multiple

949 comparison. **(F)** Images of recycling tubules in A431 cells treated or not with MβCD. Scale bars =

950 5 and 0.5 µm respectively. **(G)** Entry of GM1 C16:0 or C16:1$^{\Delta9}$ into recycling tubules in

951 cholesterol depleted A431 cells as indicated. Mean grey values of fluorescent GM1 in both

952 endosomal vesicle as well as tubule was recorded and the ratio of GM1 fluorescence in tubule

953 over vesicle was calculated for each condition. Each dot represents one tubule vs vesicle ratio.

954 Mean ± SEM. **** p = < 0.0001 by One-way ANOVA and Tukey's multiple comparison.
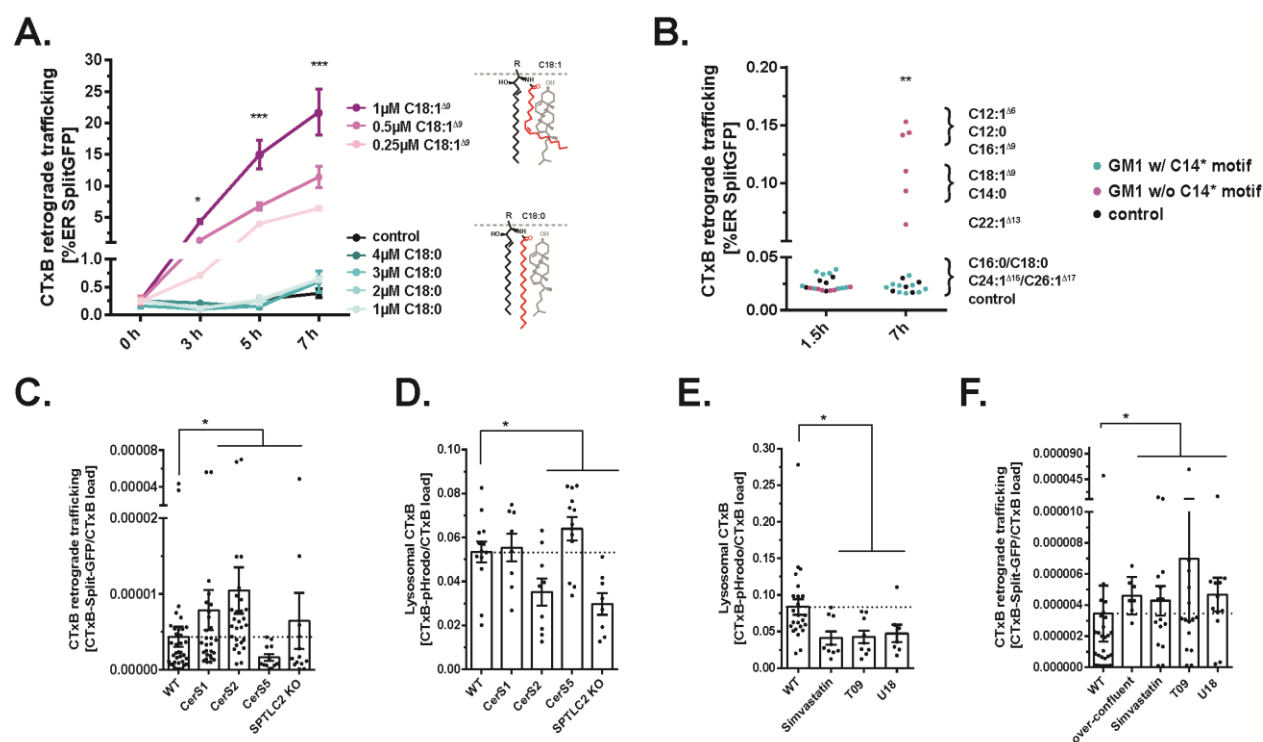
38

955

Fig. 3. Ceramide-dependent sorting into the retrograde pathway. (A) Time course of retrograde GM1 trafficking to the ER by a SplitGFP based FACS assay Graph dots represent the mean ± SD of 2 biological replicates measuring 20,000 cells each. **** p = < 0.0001 by One-way ANOVA and Tukey's multiple comparison. **(B)** SplitGFP assay as in (A) loaded with different GM1 species. Graph dots represent the mean ± SEM of 2 biological replicates measuring 20,000 cells each. **(C)** A431 CRISPR-Cas9 KO cell lines for different ceramide synthases stably expressing ER-SplitGFP.. Dot represents mean of 3 biological replicates. Mean ± SEM. **** p = < 0.0001 by One-way ANOVA and Tukey's multiple comparison. **(D)** FACS assay measuring lysosomal transport of GM1-CTxB-pHrodo™ in A431 CRISPR-Cas9 KO cell lines for different ceramide. Dot represents mean of 3 biological replicates of 20,000 cells each. Mean ± SEM. **** p = < 0.0001 by One-way ANOVA and Tukey's multiple comparison. **(E)** Lysosomal transport of GM1-CTxB-pHrodo™ in A431 WT cells mildly depleted of cholesterol as indicated. Dot represents mean of 3 biological replicates measuring 20,000 cells each. Mean ± SEM. **** p = < 0.0001 by One-way ANOVA and Tukey's multiple comparison. **(F)** A431 WT cells were mildly depleted of cholesterol as indicated and retrograde transport was measured. Dot represents mean of 3 biological

39

971   replicates measuring 20,000 cells each. Mean ± SEM. **** p = < 0.0001 by One-way ANOVA and

972   Tukey's multiple comparison.

973
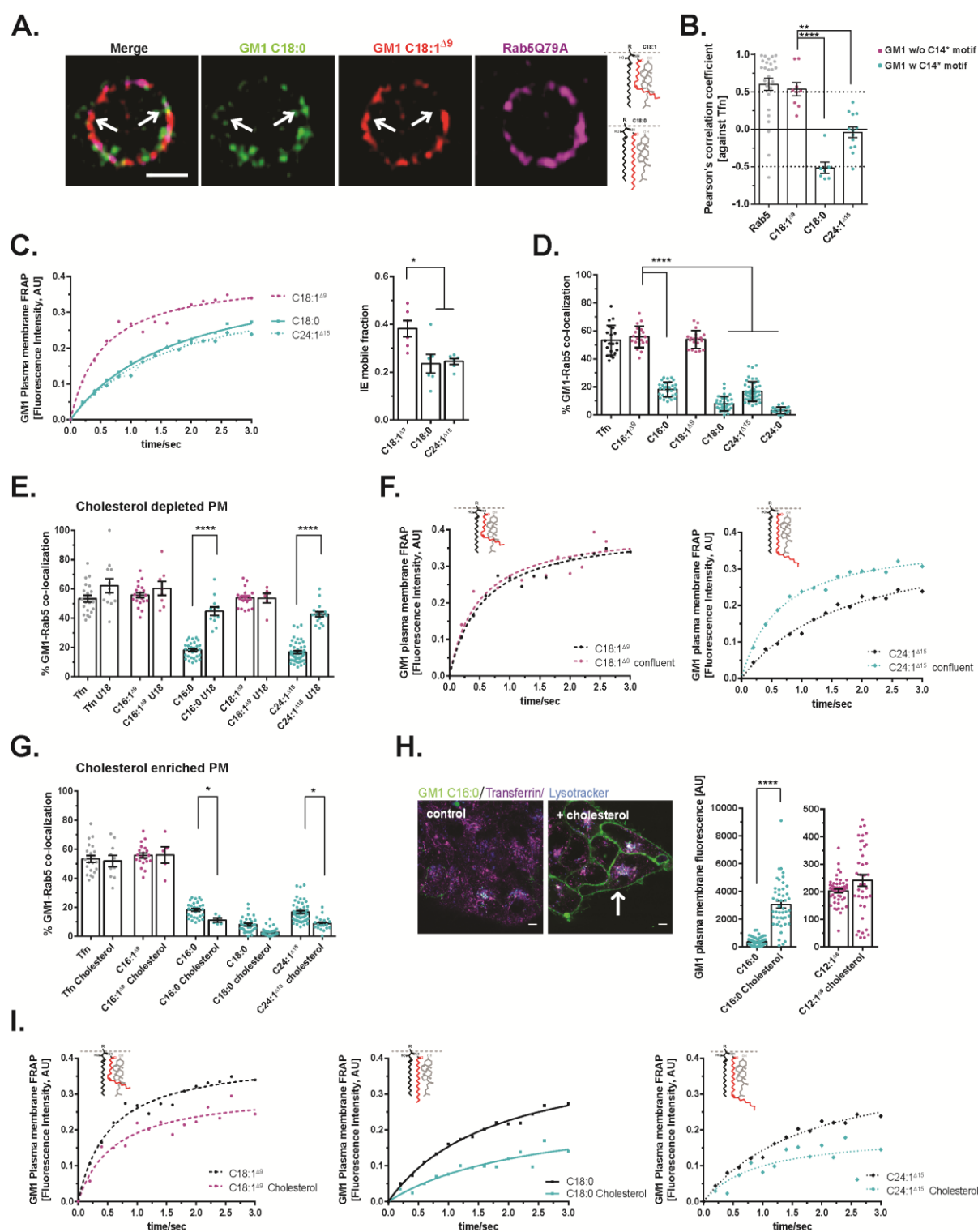
974 **Fig. 4. C14* motif drives GM1 segregation in endosomes and at the plasma membrane. (A)**

975 GM1 C18:0 (green) and GM1 C18:1$^{\Delta 9}$ (red) were incorporated into A431 cells transfected with

976 dominant active RAB5Q79L-GFP plasmid (magenta). Scale bar = 1 µm. **(B)** Pearson's correlation

977 coefficient against Tfn. Dot represents Pearson's correlation coefficient for one enlarged RAB5

978 early endosome. GM1 species with C14* motif are displayed in turquoise and GM1 species

979 without C14* motif in magenta. **** p = < 0.0001 by One-way ANOVA and Tukey's multiple

980 comparison.. **(C)** A431 WT cells were incorporated with the respective GM1 species and a

981 plasma membrane ROI was photobleached immediately. Left panel: Fluorescence recovery

982 after bleaching (FRAP) was recorded and mean grey values of one representative experiment

983 are displayed. Right panel: Quantification of IE mobile fraction for FRAP experiments. Dot

984 represents mean grey fluorescence for one FRAP experiment. Mean ± SEM. **** p = < 0.0001

985 by One-way ANOVA and Tukey's multiple comparison. **(D)** Fluorescently labeled GM1 species

986 were incorporated into genome edited SVGA cells expressing RAB5-GFP. GM1 - RAB5-GFP

987 double positive vesicles were quantified. Mean ± SEM. **** p = < 0.0001 by One-way ANOVA

988 and Tukey's multiple comparison. **(E)** as in (D), but SVGA cells were mildly cholesterol depleted.

989 **** p = < 0.0001 by One-way ANOVA and Tukey's multiple comparison. **(F)** as in (C) but A431

990 cells were grown to over-confluency. **(G)** as in (D) but genome edited SVGA cells were

991 incorporated exogenous cholesterol. Mean ± SEM. **** p = < 0.0001 by One-way ANOVA and

992 Tukey's multiple comparison. **(H)** Left panel: GM1 C16:0 (green) was incorporated into HT29

993 cells. GM1 trafficking was observed 30 min post loading in control cells or cholesterol treated

994 cells. Scale bar = 1 µm. Right panel: Quantification of plasma membrane fluorescence of GM1

995 C16:0 and C12:1$^{\Delta 6}$ incorporated into HT29 WT cells untreated or treated with exogenous

996 cholesterol. Mean grey values of cell outlines for GM1 fluorescence were measured. Dot

997 represents mean grey fluorescence for one cell outline. Mean ± SEM. **** p = < 0.0001 by One-

998 way ANOVA and Tukey's multiple comparison. **(I)** as in (C) but A431 cells were treated with

999 exogenous cholesterol.
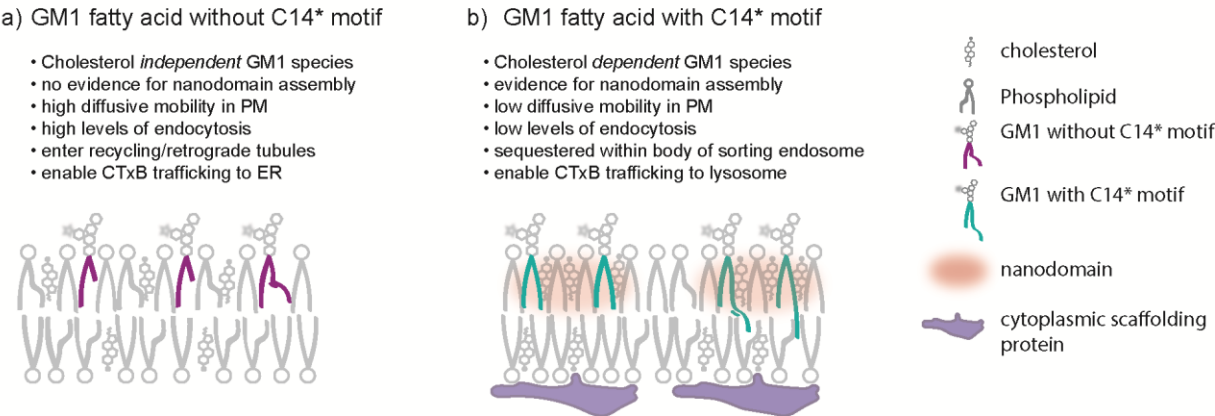
Fig. 5. Model for cholesterol-ceramide structure based GM1 sorting. a) GM1 species with short or unsaturated acyl chains (≤ C14:0 or C22:1$^{\Delta13}$) lacking the C14* motif (magenta) are unable to assemble with cholesterol into membrane nanodomains. Their membrane and endocytic trafficking phenotypes are therefore independent of membrane cholesterol. b) GM1 species with long or very long unsaturated acyl chains (≥ C16:0 and C24:1$^{\Delta15}$) containing the C14* motif (turquoise) allow for close packing with cholesterol and therefore assembly into membrane nanodomains (or rafts).

1010 **Supplementary Figures.**
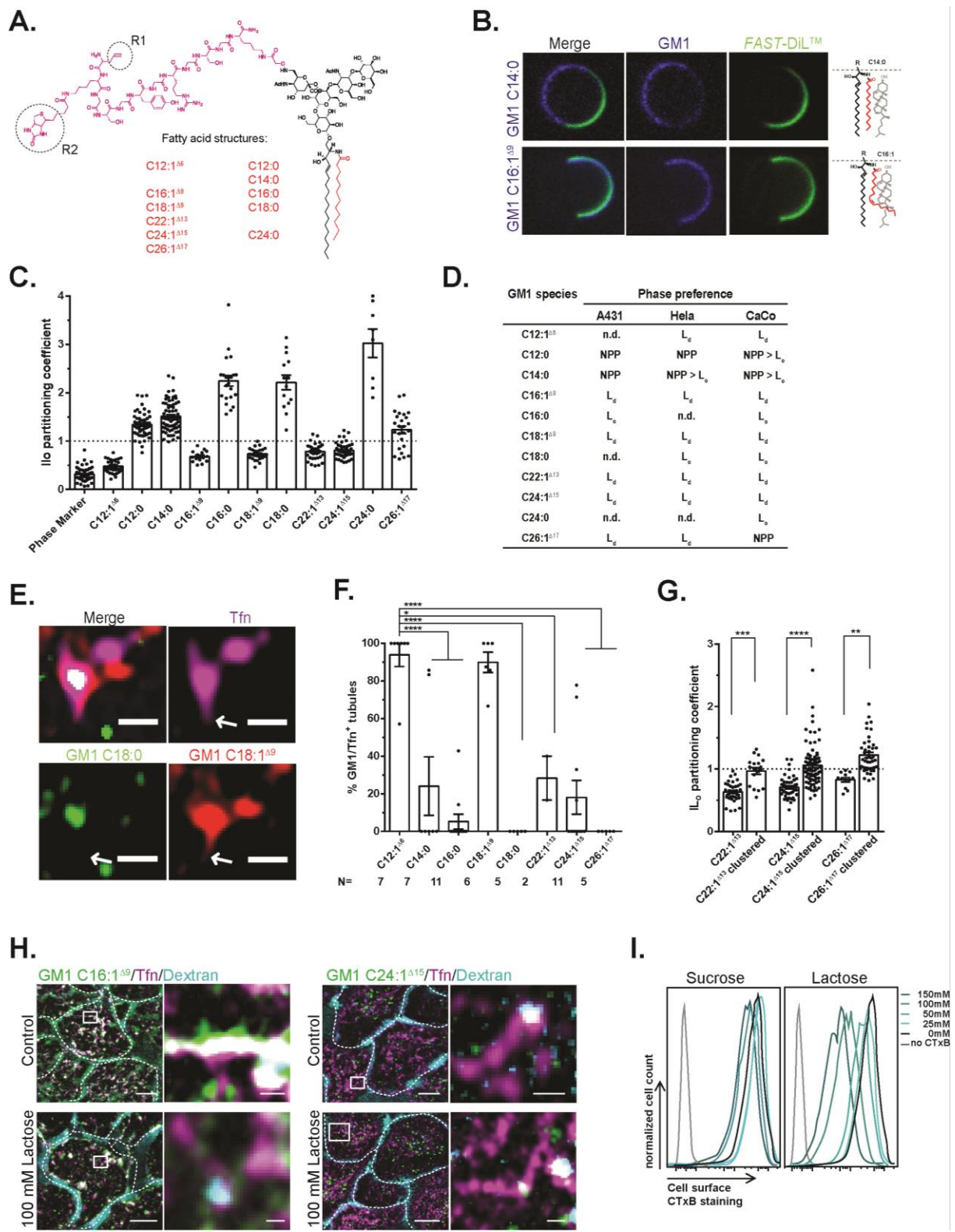
1012 **Suppl. Fig. 1. Ceramide structure specific biophysical behavior and cellular sorting of GM1. (A)**

1013 Structure of the linker 'reporter' peptide (magenta) coupled to the sialic acid of GM1

1014 oligosaccharide (black) with functional biotin (R2) for streptavidin-AlexaFluor™ detection and

1015 alkyne group (R1) for direct AlexaFluor™ azide conjugation. Sialic acid is also used for direct
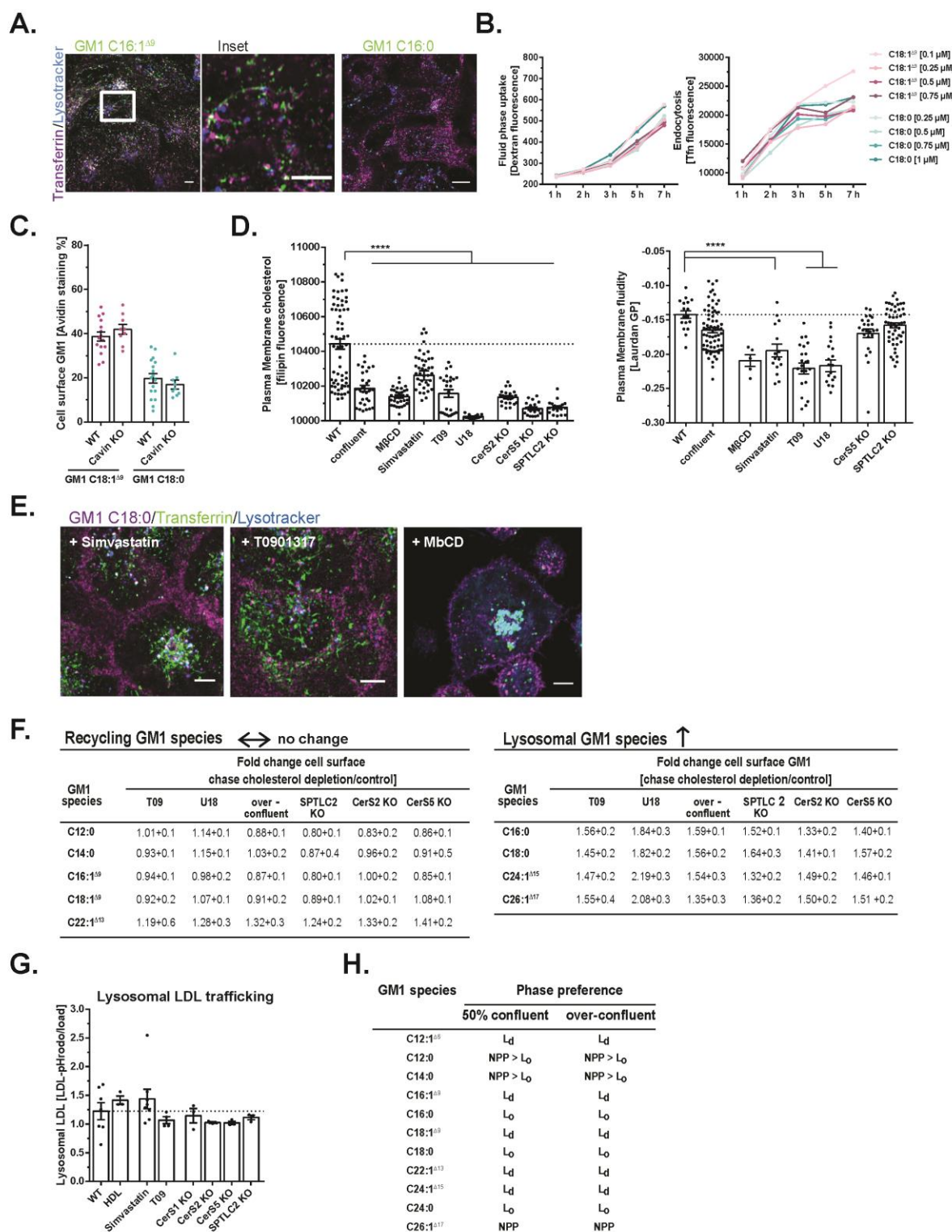
1016 AlexaFluor™ - GM1 conjugates. Different fatty acyl chain structures used in the study are

1017 displayed in red. **(B)** GPMV from CaCo BBE WT cells loaded with fluorescent GM1 C14:0 and

1018 C16:1$^{\Delta 9}$ and *FAST*-DiL™ phase marker. Exemplary images shown. **(C)** Phase preference (IL_o

1019 partitioning coefficient) for the library of GM1 species. Dot represents IL_o partitioning

1020 coefficient for one GPMV. Dotted line represents switch between IL_D and IL_O phase preference.

1021 N = ≥ 8 experiments. **(D)** Summary table for phase preference in the different cell lines. **(E)** GM1

1022 C18:0 (green) and GM1 C18:1$^{\Delta 9}$ (red) were concomitantly incorporated into the plasma

1023 membrane of Hela cells. Scale bar = 1 μm. **(F)** Quantification of GM1 presence in Tfn positive

1024 recycling endosomal tubules of Hela cells as for Fig. 1E. Mean ± SEM. **** p = < 0.0001 by One-

1025 way ANOVA and Tukey's multiple comparison. **(G)** Phase preference of different GM1 species,

1026 directly fluorescently labeled or clustered by fluorescently labeled CTxB. Dot represents IL_o

1027 partitioning coefficient of 1 GPMV, n = ≥ 4 experiments. **** p = < 0.0001 by One-way ANOVA

1028 and Tukey's multiple comparison. **(H)** Endosomal sorting of GM1 C16:1$^{\Delta 9}$ or GM1 C24:1$^{\Delta 15}$

1029 (green) was monitored in A431 cells in the presence or absence of 100 mM lactose, and

1030 transferrin (magenta) and dextran (blue) as in Fig.1C. Scale bars = 5 μm and 0.5 μm respectively.

1031 **(I)** FACS sorting of A431 cells incubated with 5 nM fluorescently labeled CTxB in the presence of

1032 indicated amount of sucrose or lactose. Cells were then FACS sorted to measure CTxB binding

1033 to the cell surface. Lines represent fluorescence of 20,000 cells sorted.

1034

F.

Recycling GM1 species ⟷ no change

GM1 species	Fold change cell surface [chase cholesterol depletion/control]					
	T09	U18	over - confluent	SPTLC2 KO	CerS2 KO	CerS5 KO
C12:0	1.01+0.1	1.14+0.1	0.88+0.1	0.80+0.1	0.83+0.2	0.86+0.1
C14:0	0.93+0.1	1.15+0.1	1.03+0.2	0.87+0.4	0.96+0.2	0.91+0.5
C16:1Δ9	0.94+0.1	0.98+0.2	0.87+0.1	0.80+0.1	1.00+0.2	0.85+0.1
C18:1Δ9	0.92+0.2	1.07+0.1	0.91+0.2	0.89+0.1	1.02+0.1	1.08+0.1
C22:1Δ13	1.19+0.6	1.28+0.3	1.32+0.3	1.24+0.2	1.33+0.2	1.41+0.2

Lysosomal GM1 species ↑

GM1 species	Fold change cell surface GM1 [chase cholesterol depletion/control]					
	T09	U18	over - confluent	SPTLC 2 KO	CerS2 KO	CerS5 KO
C16:0	1.56+0.2	1.84+0.3	1.59+0.1	1.52+0.1	1.33+0.2	1.40+0.1
C18:0	1.45+0.2	1.82+0.2	1.56+0.2	1.64+0.3	1.41+0.1	1.57+0.2
C24:1Δ15	1.47+0.2	2.19+0.3	1.54+0.3	1.32+0.2	1.49+0.2	1.46+0.1
C26:1Δ17	1.55+0.4	2.08+0.3	1.35+0.3	1.36+0.2	1.50+0.2	1.51 +0.2

G.

Lysosomal LDL trafficking

H.

GM1 species	Phase preference	
	50% confluent	over-confluent
C12:1Δ6	Ld	Ld
C12:0	NPP > Lo	NPP > Lo
C14:0	NPP > Lo	NPP > Lo
C16:1Δ9	Ld	Ld
C16:0	Lo	Lo
C18:1Δ9	Ld	Ld
C18:0	Lo	Lo
C22:1Δ13	Ld	Ld
C24:1Δ15	Ld	Ld
C24:0	Lo	Lo
C26:1Δ17	NPP	NPP

1035

1036 **Suppl. Fig. 2. Cholesterol dependent sorting into lysosomal pathway. (A)** Flu GM1 C16:1^{Δ9}

1037 (green) and C16:0 (green) were loaded into A431 WT cells and trafficked with transferrin

1038   (magenta) and lysotracker (blue) for 6 h. Recycling endosomal tubules were visualized (Inset).

1039   Scale bar = 5 and 1 μm respectively. **(B)** Different concentrations of GM1 C18:1$^{\Delta 9}$ and GM1

1040   C18:0 were incorporated into A431 cells. GM1 species with C14* motif are displayed in

1041   turquoise and GM1 species without C14* motif in magenta. Transferrin and dextran were

1042   added during the 'chase' period to monitor fluid phase uptake by FACS. Dot represents mean of

1043   2 biological experiments measuring 20,000 cells each. **(C)** GM1 C18:1$^{\Delta 9}$ and GM1 C18:0

1044   recycling was measured in A431 WT cells or CRISPR-Cas9 KO cells for CAVIN-1 as in (Fig. 1A).

1045   Dot represents mean of 2 biological experiments measuring 20,000 cells each. Unpaired t-test

1046   was performed. **(D)** A431 WT control cells and cells treated to mildy lower cholesterol were

1047   fixed and stained for plasma membrane cholesterol quantification using filipin III (left panel).

1048   Cell outlines were detected and mean grey values plotted. Right panel: Membrane fluidity was

1049   measured in GPMVs obtained from control and treated cells using laurdan. Each dot represents

1050   the general polarization (GP) value for one GPMV. Mean and SEM. **** $p = < 0.0001$ by One-

1051   way ANOVA and Tukey's multiple comparison. **(E)** GM1 C18:0 (magenta) was incorporated into

1052   A431 cells treated as indicated. Tfn (green) and lysotracker™ (blue) were added to demark

1053   integrity of intracellular organelles. **(F)** Tabularized summary of plasma membrane recycling for

1054   different GM1 species under respective cholesterol lowering conditions as in Fig. 2D. Fold

1055   change of GM1 amount at the plasma membrane in treated over control conditions are

1056   displayed. ** $p = < 0.01$ or n.s. by One-way ANOVA and Tukey's multiple comparison. **(G)**

1057   Lysosomal trafficking of pHrodo™-labeled LDL by FACS for A431 cells untreated or treated as

1058   indicated (as in D and F). Dot represents mean of 2 biological experiments with 20,000 cells

1059   each. Mean ± SEM. One-way ANOVA and Tukey's multiple comparison. **(H)** Phase preference

1060   was quantified different GM1 species in A431 cell GPMVs at 50% confluency or grown to over-

1061   confluency for 48 h.

1062
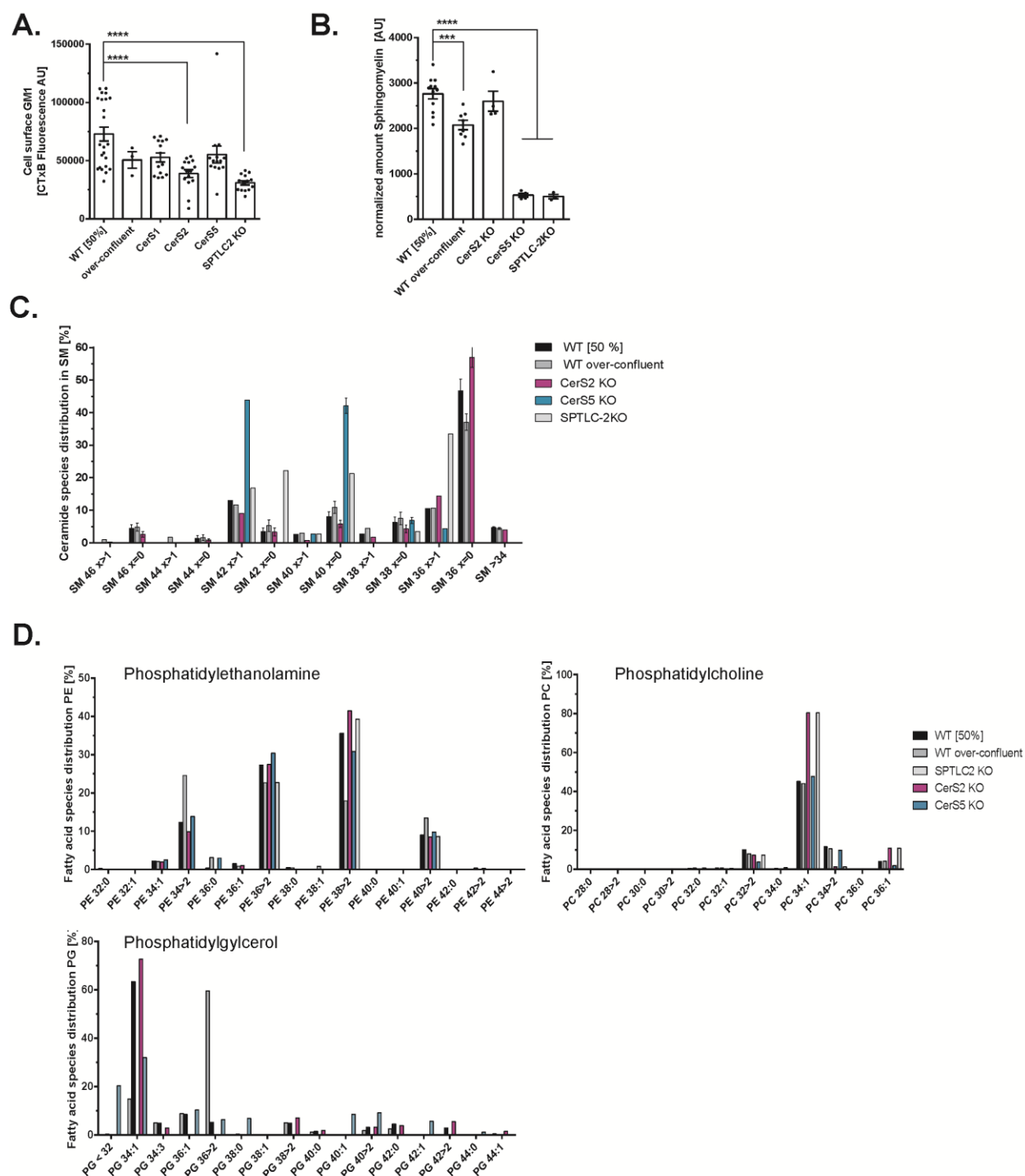
Suppl. Fig. 3. Lipidomic profiling of A431 WT and ceramide synthase KO cell lines. (A) CTxB surface staining for GM1 amount in A431 WT or CRISPR-Cas9 KO as indicated. Mean ± SEM. Dot represents mean of 2 biological experiments measuring 20,000 cells each. **** $p = < 0.0001$ by One-way ANOVA and Tukey's multiple comparison. **(B)** Sphingomyelin amount of lipidomics

1067   profiling for A431 WT, over-confluent and CRISPR-Cas9 KO as indicated. Mean ± SEM. **** p =

1068   < 0.0001 or *** p = < 0.001 by One-way ANOVA and Tukey's multiple comparison. **(C)** Ceramide

1069   profile of sphingomyelin species in % for A431 WT, over-confluent and CRISPR-Cas9 KO as

1070   indicated. N = > 4 biological replicates. (D) Phosphatidylcholine (PC), - glycerol (PG) and −

1071   ethanolamine (PE) fatty acid profiles in % for A431 WT, over-confluent and CRISPR-Cas9 KO as

1072   indicated.

1073
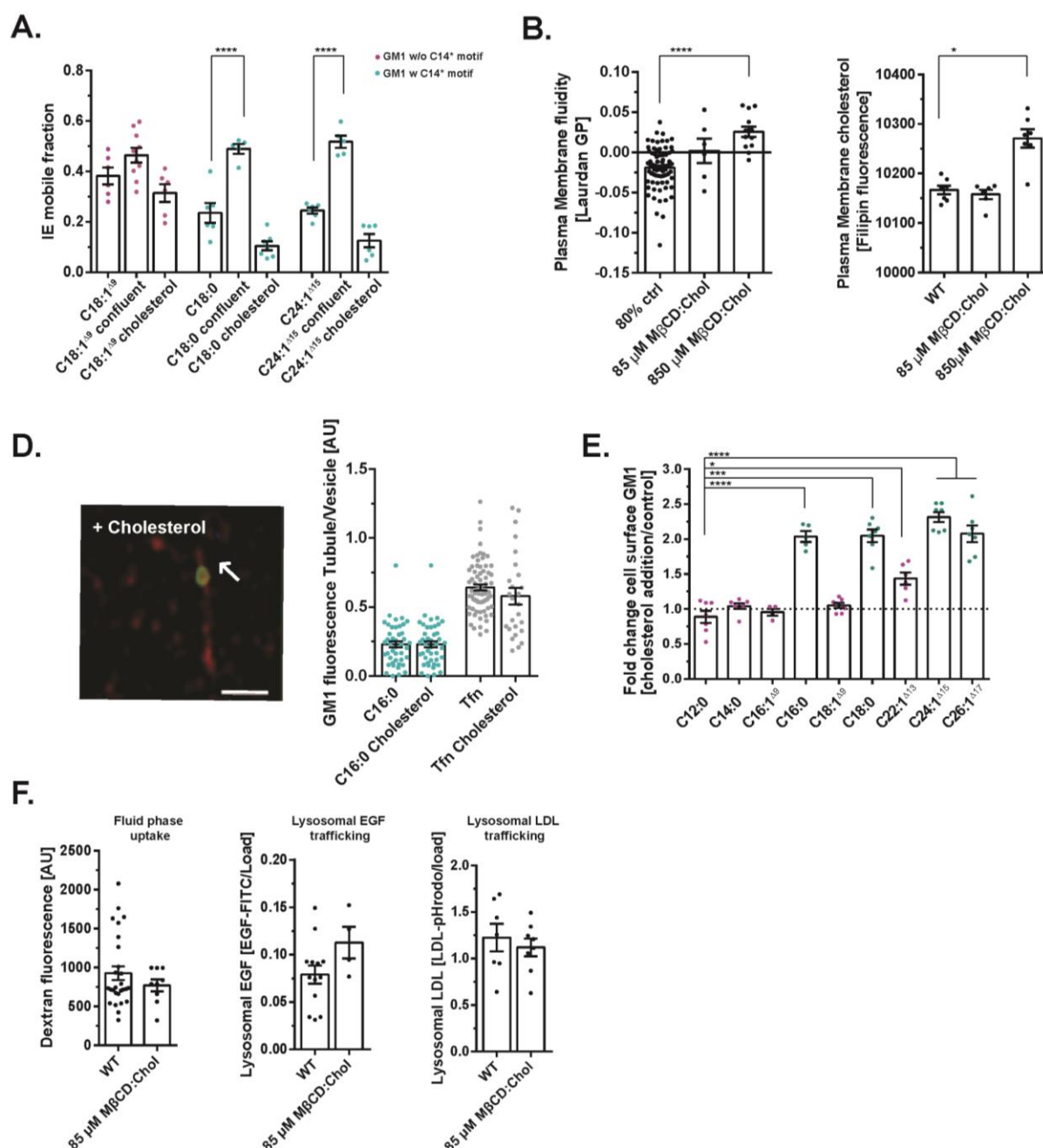
1074 **Suppl. Fig. 4. Plasma membrane nanodomain behavior of different GM1 species. (A)**

1075 Quantification of IE mobile fraction for FRAP experiments in Fig. 4C, F and I. Dot represents

1076 mean grey fluorescence for one FRAP experiment. Mean ± SEM. **** $p = < 0.0001$ by One-way

1077 ANOVA and Tukey's multiple comparison. **(B)** Left panel: Filipin staining of plasma membranes

1078 of A431 WT cell treated with exogenous cholesterol or untreated. Right panel: Laurdan staining

1079 of GPMVs produced from A431 control or cholesterol treated A431 cells Dot represents mean

1080 of 2 biological replicates or one GPMV respectively. Mean ± SEM. **** $p = < 0.0001$ or * $p = <$

1081 0.05 by One-way ANOVA and Tukey's multiple comparison. **(D**) Left panel: GM1 C16:0 (green)

1082 and transferrin (red) were added to A431 cells treated with exogenous cholesterol. Right panel:

1083 Ratio of GM1 C16:0 and Tfn in recycling endosomal tubules over its respective vesicle. Dots

1084 represent 1 tubule to vesicle ratio. Mean ± SEM. One-way ANOVA and Tukey's multiple

1085 comparisons were performed. **(E)** FACS based recycling assay for linker-peptide labeled GM1

1086 species in cholesterol treated A431 cells. Fold change between treatment and control is

1087 plotted. Dot represents mean of two biological replicates measuring 20,000 cells. Mean ± SEM.

1088 **** $p = < 0.0001$, *** $p = < 0.001$, * $p = < 0.05$ by One-way ANOVA and Tukey's multiple

1089 comparison. **(F)** Left panel: dextran fluid phase uptake by FACS was measured in A431 WT cells

1090 treated with exogenous cholesterol or untreated. Center and right panel: Lysosomal EGF and

1091 LDL trafficking in A431 WT cells treated with exogenous cholesterol or untreated using FITC-EGF

1092 and pHrodo™-LDL. Dot represents mean of two biological replicates measuring 20,000 cells.

1093 Mean ± SEM. One-way ANOVA and Tukey's multiple comparisons were performed to test

1094 statistical difference. **** $p = < 0.0001$, *** $p = < 0.001$, * $p = < 0.05$ by One-way ANOVA and

1095 Tukey's multiple comparison.

1096

1097 **Supplementary Video Files**

1098 **Suppl. Video1.** Lattice lightsheet microscopy of sorting endosome containing GM1 C16:1$^{\Delta 9}$

1099 (green), transferrin (magenta) and dextran (turquoise) with sorting tubules emerging.

1100   **Suppl. Video1.** Lattice lightsheet microscopy of sorting endosome containing GM1 C18:1$^{\Delta 9}$

1101   (green), and GM1 C18:0 (magenta) with sorting tubules emerging.

1102

1103

1104